RAINCAST

WP3200 REPORT

Assessment of snowfall observation capabilities of space-borne microwave active and passive sensors

G. Panegrossi[1], M. Montopoli[1], D. Casella[1], A. Camplani[1], P. Sanò[1], L. Baldini[1], S. Laviola[1], K. Mroz[2], A. Battaglia[2]

1. CNR - Institute of Atmospheric Sciences and Climate (ISAC), Italy
2. University of Leicester, Leicester, UK

Contributions from Mark Kulie (NOAA/NESDIS), Jean-François Rysman (LMD, France)

This document is property of the RAINCAST consortium.
In response to ITT: AO/1-9324/18/NL/NA

Table of Contents

List of acronyms

2CPC	2C-PRECIP-COLUMN
2CSP	2C-SNOW-PROFILE
AMSR-E	Advanced Microwave Scanning Radiometer for EOS
AMSR-2	Advanced Microwave Scanning Radiometer - 2
AMSU	Advanced Microwave Sounding Unit
ATBD	Algorithm Theoretical Baseline Document
ATMS	Advanced Technology Microwave Sounder
AVHRR	Advanced Very High Resolution Radiometer
CALIOP	Cloud-Aerosol Lidar with Orthogonal Polarisation
CALIPSO	Cloud-Aerosol Lidar and Infrared Pathfinder Satellite Observations
Cc	Correlation Coefficient
CONUS	CONterminous US
CPR	Cloud profiling Radar
CS	Clear Sky
CSI	Critical Success Index
DARDAR	raDAR+liDAR
dpQC	dual-polarization radar Quality Control
DMSP	Defense Meteorological Satellite Program
DPR	Dual-Frequency Precipitation Radar
EarthCARE	Earth Clouds, Aerosol and Radiation Explorer
EPS-SG	EUMETSAT Polar System- Second Generation
ERA-5	ECMWF Reanalysis 5th Generation Model
FAA	Federal Aviation Administration (USA)
FAR	False Alarm Rate
FOV	Field of View
GEO	Geostationary Earth Orbit
GFS	NOAA's Global Forecast System
GIS	Greenland Ice Sheet
GMI	GPM Microwave Imager
GPM	Global Precipitation Measurement mission
GPM-CO	Global Precipitation Measurement - Core Observatory
GOES	Geostationary Operational Environmental Satellite
GMASI	Global Multisensor Automated satellite-based Snow and Ice Mapping System
GPCC	Global Precipitation Climatology Centre
GPROF	Goddard Profiling algorithm
HADS	Hydrometeorological Automated Data System
HSS	Heidke Skill Score
ICECAPS	Integrated Characterization of Energy, Clouds, Atmospheric state, and Precipitation at Summit
IWC	Ice Water Content
IWP	Ice Water Path
Kdp	specific differential phase shift
LDA	Linear Discriminant Analysis
LEO	Low Earth Orbit
LWP	Liquid Water Path

MERRA	Modern-Era Retrospective analysis for Research and Applications
MetOp	Meteorological Operational satellite
MHS	Microwave Humidity Sounder
MM5	Fifth-Generation Penn State/NCAR Mesoscale Model
MODIS	Moderate Resolution Imaging Spectroradiometer
MQT	Office in Marquette
MRMS	Multi-Radar-Multi-Sensor
MSG	Meteosat Second Generation
MW	Microwave
MWCC	MicroWave Cloud Classification
MWI	Micro-Wave Imager
MWS	Micro-Wave Sounder
NASA	National Aeronautics and Space Administration
NESDIS	National Environmental Satellite, Data, and Information Service
NEXRAD	Next-Generation Radar
NIC	National Ice Center
NOAA	National Oceanic and Atmospheric Administration
NOHRSC	National Operational Hydrologic Remote Sensing Center
NPP	National Polar-orbiting Partnership
NWS	National Weather Service
PDF	Probability Density Function
POD	Probability Of Detection
PMW	Passive Microwave
PPS	Precipitation Processing System
PSD	Particle Size Distribution
QPE	Quantitative Precipitation Estimation
RAP	Rapid Update Cycle
R_{LF}	Low Frequency Ratio
RMSE	Root Mean Square Error
RQI	Radar Quality Index
RT	Radiative Transfer
SCE	Supercooled liquid water embedded in the cloud
SD	Snow Depth
SFR	Snowfall Rate
SI	Scattering Index
SIC	Sea Ice Concentration
SLALOM	Snow retrievaL ALgorithm fOr gMi
SLCT	Supercooled liquid water at the cloud top
S_{MRMS}	Surface snow precipitation rate
SN	Snowfall
SNODAS	SNOw Data Assimilation System
SNPP	Suomi National Polar-orbiting Partnership
SSM/I	Special Sensor Microwave - Imager
SSMIS	Special Sensor Microwave - Imager/Sounder
SSR	Surface Snowfall Rate
SWE	Snow Water Equivalent
SWP	Snow Water Path
T2m	2 meter wet bulb Temperature
TB	Brightness Temperature
TCR	Tropical/Convective Rain mix

TCWV	Total Column Water Vapour
TELSEM2	Tool to Estimate Land-Surface Emissivities at Microwave-2
TSR	Tropical/Stratiform Rain mix
UTC	Coordinated Universal Time
WSR	Warm Stratiform Rain
WSR-88D	U.S. operational Weather Surveillance Radar-1988 Doppler
WV	Water Vapour

0. Work package objective

This WP3200 is dedicated to the assessment of snowfall observation capabilities of the currently available most advanced space-borne passive microwave (MW) sensors (GMI and ATMS) and space-borne radars (DPR and CPR) through the exploitation of satellite-based and ground-based observational datasets. The goal of the WP is to contribute to the goal of the RainCast study (i.e., to provide criteria and guidelines in the design of future missions dedicated to global precipitation monitoring), by: 1) critically reporting on the different scientific aspects and on the complexity related to global snowfall detection and quantification, 2) analyzing in detail and providing evidence of such complexity, and 3) proposing observation and retrieval strategies to be adopted in the future to improve detection and quantification snowfall, with particular focus on higher latitudes.

The Report is based both on a review of all recent studies on satellite snowfall observation and on the research carried out within the WP during the project.

1. Introduction

Retrieving snowfall from space is necessary to globally quantify water resources (Levizzani et al., 2011, Skofronick-Jackson et al., 2019). Recent research provides some initial indications that precipitation has been increasing but verifying or accurately quantifying the magnitudes of these changes is difficult due to little in situ data (Surussavadee and Staelin, 2009). In particular, high latitudes regions have experienced, and are experiencing, significant changes brought about by climate change. While the effect on temperatures is relatively well known, the impact on precipitation is less well documented and understood. This is especially true in the high-latitude regions where observations and measurements are sparse and the processes poorly known. In polar regions, precipitation is dominated by shallow, low intensity, mixed-phased precipitation (Pettersen et al., 2018, 2020), but inter-dispersed with intense weather systems such as Polar Lows (Rasmussen and Turner, 2003) and other high-impact systems (Hanesiak et al. 2009). Very little is known of either extreme due to the paucity of existing measurements and the dissimilarity with precipitation observed elsewhere over the globe: this has the potential to impact forecasts of rapidly developing intense snowfalls in polar mesocyclones over maritime and coastal environments.

Spaceborne microwave (MW) sensors are particularly suitable to detect and quantify snowfall and light precipitation thanks to their unique ability to probe within clouds (e.g., Skofronick-Jacskon et al., 2004, 2013). However, remote sensing of snowfall remains among the most challenging tasks in global precipitation retrieval (Bennartz and Bauer 2003; Skofronick-Jackson et al. 2004; Noh et al. 2009, Levizzani et al., 2011, Kongoli et al. 2015, Wen et. al, 2016, Chen et al., 2016, You et al., 2016, Kulie et al., 2016, Panegrossi et al., 2017, Rysman et al., 2018, Takbiri et al., 2019, Skofronick-Jackson et al. 2019, among many others).

1.1 Spaceborne radars

Spaceborne radars, although not specifically designed to comprehensively characterize global snowfall, offer a valuable source of consistent measurements to be used as reference or to verify passive sensors' capabilities to observe falling snow. On one hand, cloud-oriented missions such as CloudSat (Stephens et al., 2008) [and EarthCARE (Illingworth et al., 2015)in the near future] offer greater sensitivity thanks to their W-band (94 GHz) cloud profiling radar (CPR) that allows to observe the vertical distribution of hydrometeors and to retrieve surface snowfall (Liu, 2008, Kulie and Bennartz, 2009, Hiley et al., 2011, Chen et al., 2016, Wood et al., 2013, 2014). CloudSat has provided unprecedented data sets for the study of clouds and global snowfall up to 82° of latitude (e.g., Behrangi et al., 2016, Kulie et al., 2016, Milani et al., 2018, Palerme et al., 2014), including unique snowfall modes (e.g. cumuliform snow, Kulie and Milani, 2018), that were previously unavailable from observational means on a near-global scale. The high frequency of the CPR is particularly suitable for observing light snowfall (Cao et al., 2014, Norin et al., 2015, Bennartz et al., 2019). However, their vertical profiles of snow are contaminated by ground clutter in the lowest 1000 m (Bennartz et al., 2019, Palerme et al., 2019, Matrosov, 2019, Milani et al., 2018), and their limited swath (with a revisiting time of 16 days for a square of 100 x 100 km^2) does not provide the needed coverage for snowfall global monitoring. On the other hand, dual-frequency radar observations are especially valuable in ice/snow cloud conditions since the scatterers are complex with large variability in microphysical properties (e.g., density, size, shape) and the interpretation of single frequency radar observations is challenging (Szyrmer et al., 2012). However, the currently available GPM-CO DPR (Ku- and Ka-band) is insensitive to the light and/or shallow precipitation that dominates the middle and higher latitudes. Casella et al. (2017) have shown that DPR detects only 5-7 % of the global snowfall events with respect to CloudSat, while 29-34 % of the CPR global snowfall mass is detected by DPR (version 4 products). They also showed that by optimally combining the dual-frequency signal (Ku and Ka band), DPR snowfall detection can increase significantly (up to 54-59% of the CPR snowfall mass). The GPM-CO DPR provides dual-frequency radar observations only between 65°N-S. Thus, there is no dual wavelength, precipitation-oriented mission over the high-latitude regions where solid precipitation dominates. Casella et al. (2017) reported about 35,000 snowfall profiles in the matched GPM-CloudSat dataset composed of the first 14 months of the GPM mission; such profiles are mostly confined to latitudes exceeding 60°N because of the combination of GPM sampling frequency near its latitudinal apex (65°N) and a CloudSat Northern Hemispheric observational bias due to CloudSat daytime-only operations since 2011. The matched GPM/CloudSat dataset is therefore not entirely geographically representative of global snowfall. Tang et al. (2017) report that the DPR observes snowfall events in some regions more effectively than the CPR (e.g., some mountainous regions), presumably because of DPR scanning capabilities compared to CPR nadir-only observations, and DPR shows a much broader latitudinal snowfall distribution compared to CPR. However, this latitudinal feature is probably due to phase discrimination disparities between the two datasets.

At W band, reflectivities for snow tend to saturate near 20 dBZ because of reduced backscattering efficiency of larger aggregates relative to lower frequencies and compensating effects of hydrometeor attenuation and multiple scattering in heavier, deeper snow events (e.g., Kuo et al. 2016; Matrosov and Battaglia 2009). DPR minimum detectable reflectivities for snow events are around 12-dBZ Ku and Ka (in HS mode). CPR and DPR were designed for very different observations: CPR for small cloud particles and DPR for precipitation-sized particles. GPM's non sun-synchronous orbit was designed to observe falling precipitation in the tropics and midlatitudes. The lower frequencies, at which the DPR operates, while necessary to avoid severe attenuation in heavier midlatitude and tropical precipitation intrinsically imply lower sensitivity. Multiple scattering and attenuation effects may partially offset each other (Matrosov and Battaglia 2009), but the relative importance of multiple scattering versus attenuation for various radar wavelengths is not yet fully quantified because of scattering and extinction uncertainties that depend on highly variable microphysical properties (e.g., snow density and size distribution) and because of three-dimensional cloud structure. The scanning nature of the DPR also reduces the dwell time, as compared to the CPR, for integration of the signal to obtain lower minimum detectable reflectivities. These differences in sensor requirements and resultant instrumentation design lead to differing capabilities between the DPR and the CPR to estimate light to heavy snow rates (see Figure 1.1.1).

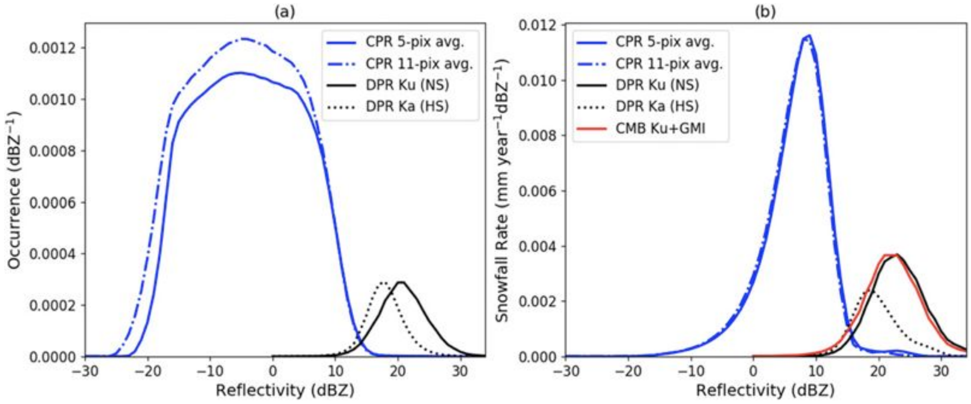

Figure 1.1.1 Probability distribution function of CPR and DPR calibrated reflectivities using data from April 2014–March 2017 for snow-only observations of Greenland Ice Sheet (a) reflectivity occurrence in dBZ-1, and (b) snowfall rate in mm year^{-1} dBZ^{-1} (*from Skofronick-Jacskon et al. 2019*).

This topic has been addressed recently by Skofronick-Jackson et al. (2019) who compared snow retrieval products from the GPM-CO satellite (version 5) and CloudSat's CPR falling snow product (release R05 of the 2C-SNOWPROFILE (Wood 2011; Wood and L'Ecuyer 2013) and identified among the causes of their differences the snow–rain classification methods, orbits, resolutions, sampling, instrument specifications, and algorithm assumptions. DPR-based algorithms use precipitation phase at the lowest radar range gate uncontaminated by surface clutter, which may be 0.5–2.0 km above the surface (even over oceans). This leads to too-frequent classification of precipitation as snowfall by these algorithms compared to CloudSat CPR snowfall product (whose phase determination is based on near-surface conditions), for example over the Gulf of Alaska, northern Atlantic south and east of Iceland, and Southern Ocean north of about 50°S. Adopting a 2-m wet-bulb temperature (T2m) surface precipitation phase classification methodology (Sims and Liu 2015) in DPR products eliminates these large surface snowfall signatures over midlatitude oceans. However, even after equalizing snow–rain classification methodologies and limiting latitudinal extent, *CPR observes nearly 10 (3) times the occurrence (accumulation) of falling snow as DPR*. The occurrence disparity is substantially reduced if CloudSat pixels are averaged to simulate DPR radar pixels and CPR observations are truncated below the 8-dBZ reflectivity threshold (which can be considered the DPR-equivalent sensitivity at W-band). However, even though the truncated CPR- and DPR-based data have similar falling snow occurrences, average snowfall rate from the truncated CPR record remains significantly higher (43%) than the DPR, indicating that retrieval assumptions (microphysics and snow scattering properties) are quite different. Diagnostic reflectivity (Z)–snow rate (S) relationships were therefore developed at Ku and W band using the same snow scattering properties and particle size distributions in a final effort to minimize algorithm differences. CPR–DPR snowfall amount differences were reduced to 16% after adopting this diagnostic Z–S approach. The authors evidenced the importance of developing multifrequency Z–S tables based on consistent microphysical and scattering assumptions when interpreting multi-frequency space-based radar observations.

1.2 Passive microwave snowfall retrieval: potentials and challenges

Passive microwave sensors appear promising for snowfall characterisation. Most of these sensors have high frequency channels (90-190 GHz) that are highly sensitive to snowfall due to the scattering by snowflakes of upwelling radiation (Bennartz and Bauer, 2003, Liu and Seo, 2013, Skofronick-Jackson and Johnson, 2011, Gong and Wu, 2017). In addition, passive microwave radiometers have a large swath and have been installed on many platforms over the last decades which ensures a good global coverage and lengthy data records. However, detection and quantification of snowfall by passive microwave observations is challenging because it involves complex and dynamic interactions between the snowfall scattering signal and the surface (Levizzani et al. 2011, You et al. 2017, Skofronick-Jackson et al. 2017). *First*, compared to rainfall, the snowfall backscattering is much weaker (Grody 1991; Kim et al. 2008; Kulie et al. 2010) and depends on more complex microphysical characteristics snowfall such as shape and density of snowflakes (Petty, 1994, Bennartz and Petty, 2001, Liu 2008, Kulie et al., 2010, Petty and Huang 2010, Skofronick-Jackson and Johnson 2011, Kuo et al., 2016, Olson et al., 2016). These characteristics are difficult to accurately parameterize and recent studies have been carried out to improve microwave and sub-millimetre single scattering properties parameterization of complex ice particles (Eriksson et al, 2018, Ekelund and Eriksson, 2019, Kneifel et al., 2020). *Second*, the already weak snowfall scattering signal tends to be masked by the increased atmospheric emissivity and liquid water content in precipitating conditions (Kneifel et al. 2010, Johnson et al., 2016, Liu and Seo 2013, Wang et al. 2013, Panegrossi et al. 2017). *Third*, changes in surface emissivity due to snow accumulation on the ground or sea ice variability can significantly alter the snowfall microwave signal (Laviola et al., 2015, Prigent et al., 2006, Noh et al. 2009, You et al., 2017, Turk et al. 2017, Munchak et al., 2020). Dry snow cover scatters the upwelling surface radiation at frequencies above 20 GHz (Ulaby and Stiles 1980; Hallikainen et al. 1987) similar to the snowfall (Grody 2008). As a result, the snowfall microwave signature gradually weakens as snow accumulates on the ground (Ebtehaj and Kummerow 2017). The snow-cover scattering evolves with time as a function of snow-cover metamorphism. For example, a small amount of liquid water content (e.g., 2%) significantly reduces the snow-cover scattering and increases its absorptivity (Stiles and Ulaby 1980; Hallikainen et al. 1986, 1987). Hence, snow cover has a time-varying effect on snowfall upwelling signal. Panegrossi et al. (2017), as well as You et al., (2017) and Ebtehaj and Kummerow, (2017), Munchak et al. (2020), and Takbiri et al. (2019) have evidenced the need to characterise the extremely variable background surface at the time of the overpass, especially at high latitudes (in cold and dry conditions), where high frequency channels are more affected by the surface emission and scattering signal.

1.3 PMW snowfall retrieval approaches

Physical and empirical approaches have been developed for passive microwave retrievals of snowfall using passive microwave radiometers, both conically scanning, such as SSM/T2 (Liu and Curry 1997), SSMIS (You et al. 2015) and GMI (You et al. 2017, Rysman et al., 2018, Takbiri et al., 2019), and cross-track scanning, such as AMSU-B/MHS (Kongoli et al. 2003, Skofronick-Jackson et al. 2004, Ferraro et al., 2005, Surussavadee and Staelin 2009, Noh et al. 2009, Liu and Seo 2013, Kongoli et al., 2003, Laviola et al., 2013) and ATMS (Kongoli et al. 2015, 2018, Meng et al., 2017).
Skofronick-Jackson et al. (2004) presented a physical method to retrieve snowfall during a blizzard over the eastern United States using high-frequency observations from the Advanced Microwave Sounding Unit B (AMSU-B) instrument. Kim et al. (2008) simulated atmospheric

profiles of a blizzard storm with the mesoscale MM5 model and a delta-Eddington-type radiative transfer (RT) model to produce a storm-scale database for snowfall retrieval using AMSU-B observations. Noh et al. (2009) used a large number of snowfall profiles from airborne, surface, and satellite radars, as well as an atmospheric RT model (Liu 1998) to generate a regional database for snowfall retrievals using the AMSU-B data. The study used the NESDIS Microwave Land Surface Emissivity Model (Weng et al. 2001) to provide surface emissivity as an input to the RT model. The largest retrieval errors were found to be over snow-covered surfaces. Empirical passive microwave snowfall retrieval algorithms largely rely on ancillary data of precipitation radar and air temperature profile. A family of these algorithms relies on thresholding the brightness temperature at different channels (e.g., Staelin and Chen 2000; Chen and Staelin 2003; Kongoli et al. 2003, Laviola et al., 2013). For example, Kongoli et al. (2015) developed a statistical approach that partitions high-frequency brightness temperatures (>89 GHz) into two distinct warm and cold weather regimes by thresholding the brightness temperature at 53 GHz. Another class of empirical approaches relies on Bayesian techniques. These techniques use a database or a lookup table that relates brightness temperatures of snowing clouds to the radar snowfall observations along with the atmospheric temperature profile. As an example, Liu and Seo (2013) used matched observations from the CloudSat Profiling Radar (CPR), the AMSU-B, and NOAA's Microwave Humidity Sounder (MHS). More recently, Sims and Liu (2015) used the CloudSat radar and multiple ground-based reanalysis data, including near-surface air temperature, atmospheric moisture, low-level vertical temperature lapse rate, surface skin temperature, surface pressure, and land cover types to diagnose precipitation phase partitioning. This algorithm is deployed in the GPM operational precipitation retrieval algorithm GPROF (Kummerow et al. 2015). GPROF is based on a Bayesian approach based on the use of a-priori database built from DPR-based precipitation profiles and ground-based radar snowfall observations. Besides GPROF, several retrieval approaches are currently based on the exploitation of the large observational databases built from the currently available spaceborne radars measurements (DPR or CPR) (e.g., Sanò et al., 2018, Casella et al., 2017, Rysman et al., 2018, 2019). In the recently developed CloudSat-based SLALOM snowfall retrieval algorithm for GMI (Rysman et al., 2018, 2019) low frequency channels, combined with auxiliary variables of the atmospheric conditions, are successfully used to characterize the environment, and are exploited towards snowfall detection, snow water path (SWP) and snowfall rate retrieval from GMI observations at higher latitudes. It is worth noting that most of these algorithms use reanalysis (wet-bulb temperature, 2-m temperature, or other near-surface parameters) for precipitation phase determination. However, the reanalysis data are often available at coarse spatial scales with significant uncertainty, which hampers the applicability for accurate detection of snowfall (Harpold et al. 2017). In a recent study, Takbiri et al. (2019) examine a prognostic Bayesian k-nearest neighbor (KNN) algorithm that strictly relies on observed passive microwave brightness temperatures and does not use any on-line reanalysis data of temperature and moisture profiles to detect overland precipitation phase. MODIS sensor data are used to account for effects of the background snow-cover emission. The algorithm shows improved skill in detection of snowfall over snow cover and can predict the likelihood of precipitation phase changes in the atmospheric boundary layer, which is not well observed by the GPM radar.

A different approach has been adopted at NOAA for precipitation retrieval and it has been recently applied to snowfall retrieval over land. It is a physically-based one-dimensional variational (1D-Var) snowfall rate (SFR) retrieval algorithm for cross-track scanning radiometers (AMSU/MHS and ATMS) (Meng et al., 2017). The NOAA SFR algorithm relies on a separate snowfall detection algorithm that is composed of a satellite-based statistical model and a set of numerical weather prediction model-based filters. Currently, the SFR product is operationally generated at NOAA.

1.4 Ground-based snowfall validation studies

The recent availability of long-term high quality ground-based snowfall measurements at specific sites around the globe equipped with a gamut of remote sensing (scanning and/or profiling radars, PMW radiometers, lidars) and in-situ sensors (Castellani et al. 2015, Petäjä et al., 2016, von Lerber et al. 2017, Lubin et al., 2020, Kollias et al., 2020) offers the opportunity:
1) to allow a rigorous statistical assessment of different satellite-based snowfall products (von Lerber et al. 2017, Matrosov , 2019,Bennartz et al. (2019));
2) to identify variable snowfall characteristics between different regions and different meteorological regimes that must be accounted for in the development of snowfall retrieval algorithms (Milani et al., 2020, Pettersen et al. 2018, 2020);
3) to provide benchmark observations that can be used to simulate current and future instrument performance and to assess trade-offs in the design of future sensors (e.g. Maahn et al. (2014)).
Long-term ground-based datasets using scanning or profiling radars offer the ability to investigate current and future instrument performance trade-offs to quantitatively assess near-surface bin selection criteria and meteorological conditions associated with surface snowfall.
Several recent studies highlight different snowfall modes both from satellite (Kulie and Milani 2018, Kulie et al. 2016, West et al. 2019) and ground-based radar perspectives (Pettersen et al. 2018, 2020). Deeper cloud structures that are characteristic of mid-latitude winter cyclones are generally easier for PMWs to detect due to strong scattering signals from ice particles and higher reflectivity values that can be detected by radars with reduced sensitivity. Shallow snowfall, however, presents unique PMW detection complexities at higher latitudes since its radiative signal can be difficult to discern over snow-covered surfaces. Depending on radar sensitivity and near-surface blind zone extent, spaceborne radars might also not detect shallow snow events because of lighter radar reflectivities and extremely shallow cloud tops (Maahn et al. 2014, Pettersen et al. 2020). Shallow convective snowfall is an important component of the total global snowfall and recent studies from Kulie et al. (2016) and Kulie and Milani (2018) have evidenced how detection and quantification of shallow convective precipitation can be very challenging. Lake-effect snow is probably one of the shallow convective snowfall types most suitable for testing remote sensing capability thanks to the availability of ground-based measurements. Passive microwave sensors show a clear signal in the high-frequency channels for intense lake-effect snow bands over the lower US Great Lakes region (Milani et al., 2020). However, comparison with the ground-based multi radar multi sensor (MRMS) snowfall measurements evidence significant inconsistencies of PMW snowfall detection and quantification for this kind of events. The Bayesian GPROF algorithm misses and underestimates intense snowfall for these cases, mostly because of poor representativeness for these types of snowfall systems in the a-priori database. In the northern U.S., Pettersen et al. (2020) presented 4 winter seasons of data from an enhanced precipitation instrument suite based at the National Weather Service (NWS) Office in Marquette (MQT), Michigan (250–500 cm of annual snow accumulation) and identified two distinct of regional snow events: *shallow snow events* with precipitation heights of less than 1500 m, often associated to cold-air outbreaks, and *deep snow events*, associated to midlatitude cyclones and frontal structures. Shallow snow events occur 2 times as often as deep events, and contribute approximately equally to estimated annual accumulation.
In the work by von Lerber et al. (2017) measurements of snow microphysics combined with large-scale weather radar observations are used to generate a snowfall ground validation dataset

over Finland. The quantitative snowfall estimates are computed by applying event specific equivalent reflectivity factor-snowfall rate (Z-S) relations, derived from ice particle microphysical properties retrieved at the University of Helsinki research station in Hyytiälä, Finland, 64 km east of the radar. In von Lerber et al. (2017), the ground-based snowfall measurements in correspondence with 26 GPM overpasses are compared with NASA GPM Microwave Imager (GMI) GPROF snowfall estimates, and significant underestimation and dependence of GPROF detection skill on cloud echo top height is shown.

Pettersen et al. (2018) present a novel method for classifying Arctic precipitation using ground based remote sensors based on five years of co-located, multi-instrument data from the Integrated Characterization of Energy, Clouds, Atmospheric state, and Precipitation at Summit (ICECAPS) (Castellani et al. (2015)). The authors distinguish between different types of snowfall events depending on the *presence or absence of condensed liquid water* in the clouds that generate the precipitation. The classification reveals two distinct, primary regimes of precipitation over the Greenland Ice Sheet (GIS). One originating from fully glaciated ice clouds over the central GIS, with unique microphysical characteristics due to the high surface elevations, and associated to large scale flow patterns, and deep, frontal cloud systems advecting up and over the southeast Greenland coast. The other from mixed-phase clouds, shallower and with characteristics typical of supercooled cloud liquid water layers, and slowly propagates from the south and southwest of Greenland.

The ICECAPS measurements have been used to assess CloudSat CPR capabilities to observe snowfall over the GIS. It is worth noting that CloudSat surface snowfall rate observations over structured terrain typically come from about 1200 m above the surface and thus do not observe precipitation processes below that altitude. The impact of CloudSat's "blind zone", where measurements are affected by ground clutter, below roughly 1200 m above ground for the high GIS is studied in Bennartz et al. (2019). Reflectivity observed at CloudSat height (1000–1500 m) is lower than the reflectivity near the surface, possibly owed to precipitation processes occurring at altitudes below 1000 m. There are also cases where the upper reflectivity is higher than the reflectivity near the surface. Cases for such events could include non-precipitating clouds around 1200 m or ice particles sublimating before they reach the surface (virga). The lower reflectivity at 1000–1500 m yields an underestimation of snowfall rate of about 20 % compared to using the reflectivity near the surface. Bennartz et al. (2019) also highlight the importance of low detectability thresholds for space-borne precipitation radar for GIS (and presumably high latitudes) snowfall. About 50 % of the total accumulation over the GIS occurs at reflectivities between −10 dBZ and +7 dBZ. A minimum radar detectability threshold should therefore be lower than −10 dBZ to accurately account for snowfall over the GIS. Using the height-corrected, clutter-cleared CloudSat reflectivities Bennartz et al. (2019) evaluate various Z–S relationships in terms of snowfall accumulation through comparison with weekly stake field observations of snow accumulation available since 2007. They find annually averaged liquid equivalent snowfall from the stake field to be between 20 and 24 cm yr^{-1}, depending on the assumed snowpack density and from CloudSat 23±4.5 cm yr^{-1}. The annual mean snowfall over the GIS inferred from CloudSat is around 35 cm yr^{-1} liquid equivalent.

The issue of ground-clutter in CPR surface snowfall rate estimates has been addressed also by Matrosov (2019) who compares estimates of (liquid-equivalent) snowfall rates from the U.S. operational Weather Surveillance Radar-1988 Doppler (WSR-88D) systems with snowfall rate retrieval from CloudSat CPR 2C-SNOW-PROFILE product during spatially extensive nimbostratus snowfall events (producing much of the snow ground accumulation over Continental U.S.) in the 2013-2016 period. For these comparisons, the ground-based radar measurements are

interpolated to closely match in space and time spaceborne radar resolution volumes *above ground clutter,* thus avoiding uncertainties in deriving near-surface snowfall rates from measurements aloft by both radar types. This approach can be probably considered more rigorous for the quality assessment of spaceborne radar snowfall product, since "surface" snowfall rates observed from CloudSat are typically taken at an altitude of 1200 m above the surface. Although typical uncertainties of both ground-based and spaceborne snowfall-rate retrieval approaches are quite high, the results show good agreement with correlation coefficients being around 0.8–0.85.
The emerging extremely variable snowfall characteristics between different regions, or for different regimes, should be taken into account in the design of future sensors and in the development of snowfall retrieval algorithms.

1.5 Report outline

This study provides a comprehensive analysis of the snowfall observational capabilities of the two benchmark space-borne PMW sensors: GMI (conically scanning, on-board the GPM-CO) and ATMS (cross-track scanning, on board Suomi-NPP and NOAA-20 satellites).
The *GMI* (Draper et al., 2015), on board the non sun-synchronous GPM-CO satellite orbiting between 65°S and 65°N, is the most advanced microwave *conically scanning radiometer* in space, in terms of both channel frequency assortment and spatial resolution. It offers the most appropriate set of microwave frequencies for precipitation retrieval, with *10 dual-polarization window channels* from 10 GHz to 166 GHz, and three single-polarization water vapour absorption channels (at 23.8 GHz and two at 183.3±3 GHz, and 183.3±7 GHz). Moreover, GMI provides PMW measurements on a 904 km wide swath, at an Earth incident angle of 52.8°, at the highest available spatial resolution, ranging from 4.4 km x 7.2 km at the high-frequency channels (> 89 GHz), to 19 km x 32 km at 10 GHz.
The *ATMS* (Kim et al., 2014), is the first of a new generation of *cross-tracking microwave sounders* launched aboard the Suomi-National Polar-Orbiting Partnership satellite in October 2011, then NOAA-20, and planned for the future JPSS series. The ATMS is the evolution of the AMSU-A, MHS, and AMSU-B sounders, with a swath of 2600 km, and angular span of 52.77° relative to nadir. During each scan the Earth is viewed at 96 different angles, sampled every 1.11°. ATMS has 22 channels, ranging from 23 to 190 GHz, providing both temperature soundings from the surface to the upper stratosphere (about 1 hPa, 45 km) and humidity soundings from the surface to upper troposphere (about 200 hPa, 15 km). Particularly, ATMS channels 1–16 provide measurements at microwave frequencies below 60 GHz and in an oxygen absorption band, and channels 17–22 are located at higher microwave frequencies above 89 GHz and in a water vapor absorption band. The beamwidth changes with frequency and is 5.2 for channels 1–2 (23.8–31.4 GHz), 2.2 for channels 3–16 (50.3–57.29 and 88.2 GHz), and 1.1 for channels 17–22 (165.5–183.3 GHz). The corresponding nadir resolutions are 74.78, 31.64, and 15.82 km, respectively. The outermost FOV sizes are 323.1 km x 141.8 km (cross-track x along-track), 136.7 km x 60.0 km, 68.4 km x 30.0 km, respectively. It covers the sounding capabilities of three predecessor sounders into a single instrumental package (Kim et al., 2014). Thus, the ATMS guarantees for the future the continuity of measurements of the first AMSU sensor (1998) gathering useful data for climatic studies, operational activities and numerical weather forecast models. The ATMS is very similar to the future European EPS-SG Microwave Sounder (MWS). These radiometers, together with the EPS-SG Microwave Imager (MWI), currently represent the only long-term possibility for global precipitation monitoring from operational satellites.
By exploiting coincident (in space and time) CloudSat CPR snowfall observations the study discusses the effects of the complex interconnection of snowfall intensity, cloud depth and

microphysical characteristics (e.g., the presence of supercooled water), and environmental conditions, on the multi-channel PMW signature. In addition, the impact of the frozen background surface conditions on the PMW snowfall signal, and the potential of the two radiometers for the frozen surface characterization, are evaluated. State-of-the art snowfall retrieval products [the GPROF (Kummerow et al., 2015) and SLALOM (Rysman et al., 2018, 2019) for GMI, and the NOAA 1D-Var snowfall retrieval algorithm for ATMS (Meng et al., 2017)], are compared to CloudSat CPR for specific case studies. The U.S. ground-based radar network snowfall measurements are also used to carry out an independent validation of all GPM-based snowfall products. The ultimate goal is to provide insights for new strategies in the design of future global precipitation missions for global snowfall monitoring. Therefore, the specific objectives for this WP3200 can be summarized as follows.

1. To extend/generate global observational datasets built from coincident ATMS and GMI and CloudSat CPR microwave measurements, including ancillary key variables for the analysis of PMW snowfall spectral signature (WP Task 3.2.1, Section 2);
2. To analyze channel response of GMI and ATMS channels to different snowfall scenarios and compare their observational capabilities (accounting for their channel assortment, spatial resolution, and viewing geometry), by exploiting case-studies with co-located space-borne radar observations and ancillary environmental variables (WP Task 3.2.2, Section 3).
3. To assess state-of-the-art MW snowfall product quality (snowfall detection and retrieval capabilities) by exploiting ground-based U.S. NEXRAD network (WP Task 3.2.3, Section 4).
4. To explore the potential of low-frequency channels of GMI and ATMS to characterize the background surface (presence of sea ice, different types of snow cover), at the time of the observation (WP Task 3.2.4, Section 5).

2. Extension of the NASA 2B-CSATGPM database

In spite of the limitations of spaceborne radars for global surface snowfall monitoring outlined in Section 1, several studies have been undertaken to assess the information contained in various PMW channel combinations for snowfall detection using spaceborne radar measurements of snowfall events globally (Panegrossi et al., 2017, You et al., 2017, Ebtehaj and Kummerow, 2017, Takbiri et al., 2019). These studies are based on the use of observational datasets built from currently available coincident spaceborne active (DPR or CPR) and passive microwave (GMI) observations. In contrast to model-driven approaches (e.g., Eriksson et al., 2015) affected by some limitations in the description of the particle's optical and bulk microphysical properties, these studies have shown that the multi-year, quasi-global, and complementary DPR and CPR measurements offer, in spite of their limitations, a unique and extensive resource to analyse spaceborne microwave radiometer precipitation observational capabilities. These studies have shown that observational datasets built from currently available coincident spaceborne active and passive microwave observations can be exploited not only to refine and develop precipitation retrieval techniques (Kummerow et al., 2015, Casella et al., 2017, Sanò et al., 2016), but also to explore and verify potentials and limitations of current and future satellite missions. For instance, in the work by You et al. (2017) a coincident GPM GMI and DPR database is analyzed to determine optimal channel combinations for snowfall detection over land. In a recent study Panegrossi et al. (2017) analysed an observational dataset built from matched GMI and CloudSat-CPR snowfall observations (mainly occurring at latitudes between 55° and 65°N). The authors provided instructive insights on microwave multi-frequency signals associated with snowfall in cold regions.

In this study two main datasets of satellite radar/radiometer coincident observations have been used to analyze the snowfall observation capabilities of ATMS and GMI.
The *first dataset* considered in this report is based on the *GPM/CloudSat coincidence dataset* (2B-CSAT-GPM product available from the GPM website[1]). The 2B-CSAT-GPM dataset includes triple coincidence of ClouSat-GPM and ATMS radiometer; these triple coincidence are golden cases for the intercomparison of the capabilities of observing snowfall of the most advanced conical and cross track MW radiometers (i.e. GMI and ATMS) (see Section 3.3). However, there are some major differences in the horizontal resolution of the two radiometers, in particular for the larger ATMS incidence angles, where ATMS reaches a resolution of 122 km (for the channels at 23.8 GHz and 31.4 GHz), while the GMI horizontal resolution is higher and constant along the swath. Therefore, a *second dataset* has been built from *ATMS and CloudSat coincident observations*, where the CPR measurements are horizontally averaged to match the ATMS resolution (see Section 2.2).
In both datasets, the latest version of CloudSat snow profile product (2C-SNOW-PROFILE) (hereafter 2CSP) (release R05) (Wood 2011; Wood and L'Ecuyer 2013) is used as the reference snowfall product. It provides estimates of snowfall characteristics for each observed profile that appears to contain snow reaching the surface. Surface snow is classified primarily by the CloudSat 2C precipitation column algorithm (2C-PRECIP-COLUMN) (2CPC) product (Haynes et al. 2013) based on the strength of the radar reflectivity in the radar bin just above the blind zone (the near-surface bin), the estimated height of the melting level above the surface, and a model for the rate of snow particle melting. If 2CPC indicates that snow at the surface is ''likely'' or ''possible'' and the melting-level height is such that the melted mass fraction at the surface is less than about 15%, the 2CSP algorithm performs a retrieval. The algorithm first retrieves estimates of vertically resolved snow PSD parameters. The retrieval is performed using a Bayesian, optimal estimation (OE; Rodgers 2000) technique applied to the reflectivity profiles, supplemented with the reanalysis temperature profiles and a priori information about snow PSDs and microphysical properties. (Wood et al. 2013, 2014). The algorithm uses the retrieved PSD profiles along with the a priori microphysical properties to determine vertically resolved profiles of snowfall rate and water content within the retrieved layer. The surface snowfall rate is estimated simply as the snowfall rate in the near-surface bin.

2.1 New GPM/CPR coincidence dataset

The GPM/CPR coincidence dataset is available from the GPM website (2B-CSAT-GPM product, Turk 2016). 2B-CSAT-GPM has been recently updated from version 1C to version 4, the main upgrades regards the inclusion of more CloudSat and GPM products and the updates of all the products to the most recent version. The 2B-CSAT-GPM version 4 dataset includes a number of products and variables summarized in Table 2.1.1. This dataset (and all GPM mission data and products) is freely available through the NASA Precipitation Processing System (PPS) data archive (https://storm.pps.eosdis.nasa.gov/storm/).

[1] storm.pps.eosdis.nasa.gov

***Table 2.1.1**: GPM/CPR dataset products and variables in 2B-CSAT-GPM*

Source	Sensor/ Model	Product	Main Variables
GPM	GMI	1C-R V5A	Brightness temperatures (TBs) (K)
GPM	GMI	GPROF V5	Surface precipitation rate (mm h^{-1}) Liquid fraction (%) Frozen precipitation rate (mm h^{-1})
GPM	DPR	2A-GPM-DPR V6	Equivalent radar reflectivity factor (Z) (dBZ)
GPM	DPR	2B-GPM-DPRGMI V6	Surface precipitation rate (mm h^{-1}) precipitation rate profile (mm h^{-1})
GPM	ATMS	1C-ATMS V5	Brightness temperatures (TBs) (K)
GPM	MHS	1C-MHS V5	Brightness temperatures (TBs) (K)
CloudSat	CPR	2B-GEOPROF V5	Equivalent radar reflectivity factor (Z) (dBZ)
CloudSat	CPR	2C-SNOW-PROFILE V5	Snow water content profile (SWC) (kg m^{-3}) Surface snowfall rate (mm h^{-1})
CloudSat	CPR	2C-PRECIP-COLUMN V5	Surface precipitation rate (mm h^{-1}) Liquid fraction (%)
CloudSat	CPR	2B-CLOUD-CLASS V5	Cloud type
CloudSat	CPR	2C-RAIN-PROFILE V5	Surface rainfall rate (mm h^{-1}) rainfall rate profile (mm h^{-1})
CloudSat	CPR	2C-ICE	Ice Water Content profile (kg m^{-3})
CloudSat	CPR	ECMWF-AUX V5	2 m temperature (T2m) (K) Surface pressure (hPa) Total precipitable water (TPW) (kg m^{-2})
CloudSat	CPR	MODIS-AUX V5	MODIS thermal channels (11 channels) 3x5 MODIS cloud mask

The 2B-CSAT-GPM version 4 has been integrated with other dataset containing information on cloud microphysics (from the DARDAR dataset) and surface sea ice and snow cover (Autosnow and SNODAS), as shown in Table 2.1.2:

Table 2.1.2: Products and variables added to the GPM/CPR dataset during Raincast.

Source	Sensor/ Model	Product	Main Variables
ECMWF	Reanalysis Model	ERA-5	2m temperature [K] Skin temperature [K] Height of the 0 degree level [m] Total Column Water vapour [kg m^{-2}]
Icare/University of Lille 1	CALIPSO/ CPR	DARDAR	Ice water content (IWC) (kg m^{-3}) Phase/microphysics classes
NOAA	Multisensor (GOES, SEVIRI, AVHRR, SSMIS)	Autosnow	Daily sea-ice and snow cover maps (global)
NOAA	Assimilation System (NWP, Satellite, airborne, ground based)	SNODAS	Snow Pack Characteristics (US only) Snow Depth, Snow Water Equivalent, Snowpack Temperature, Melted Snow, Precipitated Snow.

In particular the DARDAR (liDAR + raDAR) products are essential for the study of the effects of the supercooled liquid water droplets on the TBs (Battaglia and Delanoë, 2013; Liu and Seo 2013; You et al. 2017; Ebtehaj and Kummerow 2017, Panegrossi et al., 2017). DARDAR (Ceccaldi et al. 2013) product combines the observations of the CPR radar and of the CALIOP lidar (on-board CALIPSO) to provide insights, not only into the water phase, but also into the ice water content and ice particle effective radius, with a vertical (horizontal) resolution of 60 m [1.4 km (cross-track) 1.7 km (along track)]. Thus, for each snow measurement in the GMI-CPR coincident database, we associated a flag for cases without supercooled droplets, cases with supercooled droplets embedded in the snow cloud and cases with supercooled droplets on top of the snow cloud. It should be noted that Battaglia et Delanoë [49] suggested that some supercooled layer occurrences might be missed by DARDAR due to lidar attenuation problems. Supercooled droplets that are embedded in or on top of the snow cloud are widespread at all latitudes, representing on average about 2/3 of snowfall events, as shown in Figure 2.1.1. Therefore, the presence of supercooled water and its vertical distribution within the cloud should be considered in snowfall retrieval algorithms.

Moreover, the Autosnow and SNODAS products have been exploited in the assessment of the capabilities of GMI in identifying the frozen background surfaces (see section 5). ***The Global Automated Snow and Ice Mapping System*** (***GMASI-Autosnow***, Romanov 2017) is an algorithm developed by NASA for ice and snow cover detection developed by the NOAA National Weather Service (NWS) and National Ice Center (NIC) in order to support the hydrological simulation. It generates global and continuous snow and sea ice maps with a *spatial resolution of 0.04°* (about 4 km) and a *temporal sampling of one map per day*. The maps present four flags: snow-free land, snow cover, clear water and ice cover. It is based on the combination of data obtained by four VIS-IR sensors: AVHRR onboard METOP-A satellite, the two Imagers onboard GOES-East and GOES-West and the SEVIRI on board the geostationary MSG satellite constellation. The VIS-IR data are combined with SSMIS-DMSP microwave sensor observations in order to fill the gaps due to the lack of VIS-IR observations for some environmental situations -absence of daylight and presence of clouds. ***The SNOw Data Assimilation System (SNODAS)***(Barrett 2003, Clow et al. 2012) is a modelling and data assimilation system developed by National Operational Hydrologic Remote Sensing Center (NOHRSC) to provide the best possible estimates of snow cover and associated parameters (Snow Water Equivalent, Snow Depth, Melted Masss, Precipitation, etc.) to support hydrologic modelling and analysis. The aim of SNODAS is to provide a physically consistent framework to integrate snow data from satellite, airborne platforms, and ground stations with model estimates of snow cover. The dataset covers the *contiguous United States*, from a Southernmost Latitude of 24 ° to a Northernmost Latitude of 54 °, and for a Westernmost Latitude of -131 ° to a Easternmost latitude of 62 °, with a *temporal resolution of one day* - data are referred to 6:00 U.T.C. -and a spatial resolution of 1 km.

Some of the main characteristics of the GPM/CPR dataset are summarized in Table 2.1.3. The time frame included in this dataset is limited by the start of the operational phase of the GPM and by the reprocessing of the CPR products to version 5 that is currently ongoing and, at the time of writing this report, reached the beginning of September 2016.

Table 2.1.3: GPM/CPR dataset summary.

Period	10/03/2014 – 01/09/2016
Geographical area	65 °S–65° N, 180° W–180° E
Number of coincidence	6,502
Number of triple coincidences (GPM-CPR-ATMS)	5,801
Number of CPR profiles	5,870,903
Number of CPR profiles with snowfall	400,145
Number of CPR profiles with snowfall and supercooled droplets	289,905
Horizontal resolution	1.2 km CPR ; 10 km GPM
Reference precipitation product	2C-SNOW-PROFILE and 2C-PRECIP-COLUMN V05 from CPR
GMI TBs	1C-R GMI V05A

The GPM/CPR dataset is built by a large number of relatively small segments (from 960 km to 5700 km long), whose size depends on the crossing angle between the orbits of CloudSat (sunsyncronous) and GPM-Core (with a drifting orbit). The number of coincident observations between CPR and DPR depends on the latitude (i.e. higher at higher latitititiude) as shown in Figure 2.1.1, and is clearly biased in the Northern Hemisphere, due to CloudSat daytime-only operations since 2011. The snowfall observations are mostly confined to latitudes around 60°S/N because of the combination of GPM sampling frequency near its latitudinal apex (65°S/N). The matched GPM/CloudSat dataset is therefore not entirely geographically representative of global snowfall.
The zonal distribution of snowfall events in the GPM/CPR dataset (shown in red in Figure 2.1.1) is influenced by the zonal distribution of the sampling and by zonal distribution of snowfall events Moreover, the PDF of snowfall rate intensity in the dataset reflects the snowfall PDF in CPR product 2C-SNOW-PROFILE.

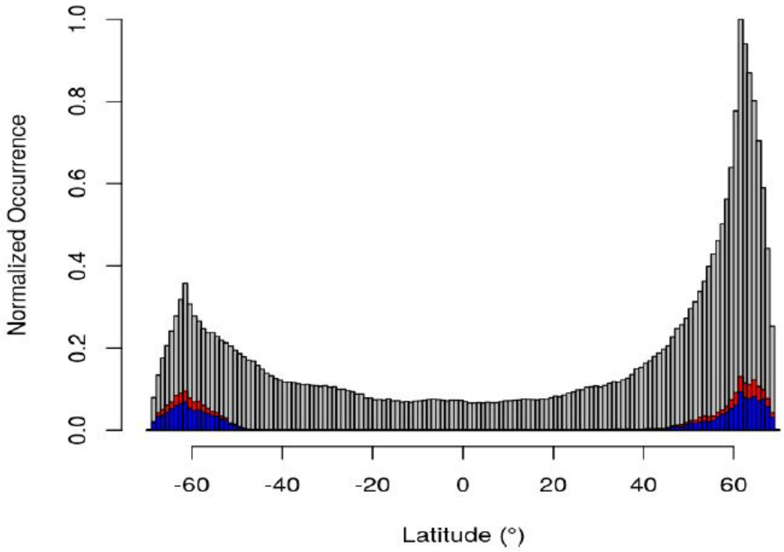

Figure 2.1.1 Zonal distribution of the GPM/CPR dataset: All (grey), snowfall (red), and snowfall with supercooled droplets (blue) [from *Rysmann et al. 2018*].

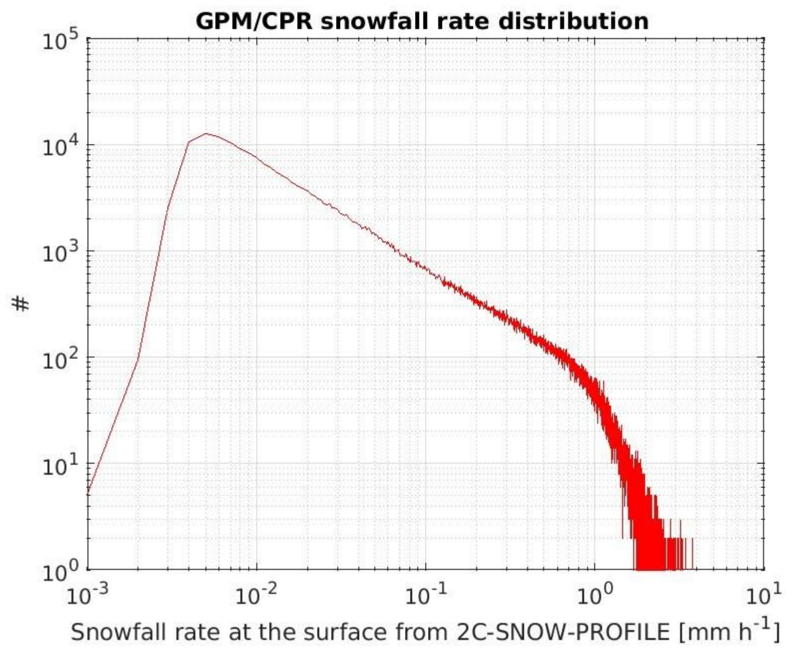

Figure 2.1.2 Snowfall rate distribution in the GPM/CPR dataset. Number of profiles (per mm/h) on the y-axis and Snowfall rate at the surface on the x axis are shown.

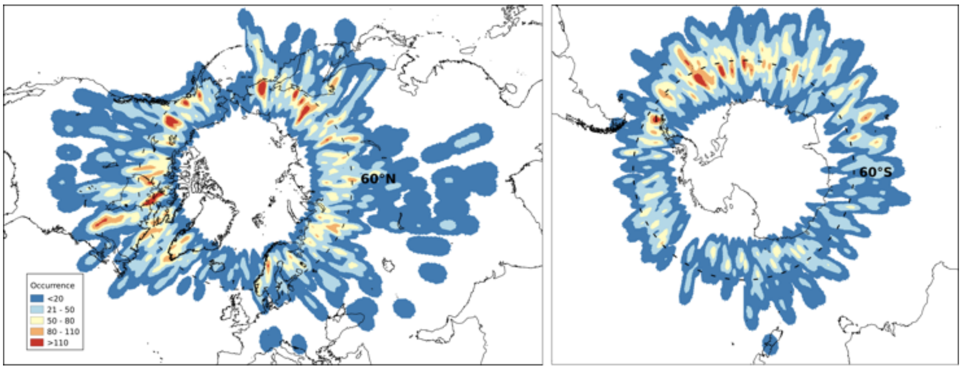

Figure 2.1.3 Map of snowfall occurences in the GPM-CPR dataset. Global distribution of snowfall elements in the GMI-CPR coincidence dataset (March 2014 - May 2016). The two panels show the number of occurrences of snowfall elements (indicated by the colors) in the Northern (left) and Southern (right) hemisphere (from *Panegrossi et al., 2017*)

2.2 New ATMS/CPR coincidence dataset

This dataset includes all the coincident observations from ATMS and CloudSat in the period between 01/01/2015 and 01/09/2016. Each coincident observation comes from observations from CPR and ATMS within a 15 minutes time window. In order to make the CPR observations comparable with ATMS in terms of horizontal resolution all the data at higher resolution (from CPR and MODIS) have been averaged with a gaussian antenna pattern to the ATMS resolution (i.e. the ATMS horizontal resolution has been calculated from the ATMS SDR ATBD[2] considering a fixed satellite height of 824 km). To account for the non-uniform beam filling effect within the ATMS pixel which is only sampled with a small stripe (about 1.7 km large) by the CPR , the MODIS cloud mask over the full ATMS pixel has been added to the dataset. Finally, some environmental variables from ERA-5 and some information on cloud microphysics from the DARDAR product and on frozen surface background from Autonsnow and SNODAS have been also added following the same procedure of the GPM/CPR dataset. Table 2.2.1 summarizes the main data included in the ATMS/CPR dataset, whereas Table 2.2.2 shows some characteristics of the dataset in terms of time and space coverage, population and horizontal resolution.

The ATMS/CPR dataset differs from GPM/CPR dataset in many aspects: the coverage is global and includes Polar regions, which are over-represented in the zonal distribution of the dataset (see Figure 2.2.1). This zonal distribution is due to the orbital geometry of CloudSat and SNPP, that are both sun-synchronous with a relatively small difference in the satellite height (i.e. about 689 km and 833 km for CloudSat and SNPP respectively). Therefore the coincidence dataset is built from longer orbit fragments (often semi orbits) and by a very large number of elements near to the poles (Fig. 2.2.2) The asymmetry between the Northern and Southern hemisphere is due to CloudSat daytime-only operations since 2011, affecting mostly the Southern Polar region. The PDF of the snowfall rate is quite different in the ATMS/CPR dataset than in the GPM/CPR dataset due to the spatial averaging at lower resolution (see Figure 2.2.3).

[2] available at https://www.star.nesdis.noaa.gov/jpss/documents/ATBD/D0001-M01-S01-001_JPSS_ATBD_ATMS-SDR_A.pdf

Table 2.2.1: ATMS/CPR dataset products and variables.

Source	Sensor/ Model	Product	Main Variables
GPM	ATMS	1C-ATMS V5	BTs[K], Latitude, Longitude, Time
CloudSat	CPR	2B-GEOPROF V5	Equivalent radar reflectivity factor (Z) (dBZ)
CloudSat	CPR	2C-SNOW-PROFILE V5	Snow water content profile (SWC) (kg m^{-3}) Surface snowfall rate (mm h^{-1})
CloudSat	CPR	2C-PRECIP-COLUMN V5	Surface precipitation rate (mm h^{-1}) Liquid fraction (%)
CloudSat	CPR	2B-CLOUD-CLASS V5	Cloud type
MODIS	MODIS	MYD35 MYD03	Modis cloud Mask (over ATMS pixel)
Icare/University of Lille 1	CALIPSO/ CPR	DARDAR	Ice water content (IWC) (kg m^{-3}) Phase/microphysics classes
ECMWF	Reanalysis Model	ERA-5	2m temperature [K] Skin temperature [K] Height of the 0 degree level [m] Total Column Water vapour [kg m^{-2}]
NOAA	Multisensor (GOES, SEVIRI, AVHRR, SSMIS)	Autosnow	Daily sea-ice and snow cover maps (global)
NOAA	Assimilation System (NWP, Satellite, airborne, ground based)	SNODAS	Snow Pack Characteristics (US only) Snow Depth, Snow Water Equivalent, Snowpack Temperature, Melted Snow, Precipitated Snow.

Table 2.2.2: ATMS/CPR dataset summary.

Period	1/01/2015 – 1/09/2016
Geographical area	90°S–90° N, 180° W–180° E
Number of ATMS orbits	3,049
Number of observations	4,670,442
Number of snowfall observations	745,533
Number of snowfall observations with supercooled droplets	456,391
Horizontal resolution (Km)	15.8 x 15.8 (nadir) 30 x 68.4 (scan edge)
Reference precipitation product	2C-SNOW-PROFILE and 2C-PRECIP-COLUMN V05 from CPR
ATMS BTs	1C ATMS V05A

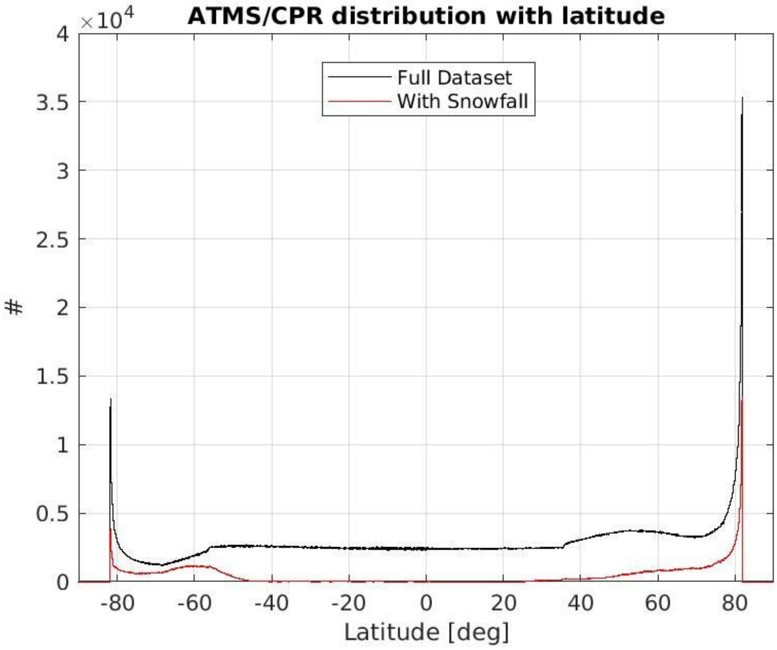

Figure 2.2.1 Distribution of the ATMS/CPR dataset (black) and of the snowfall observations in the dataset with latitude.

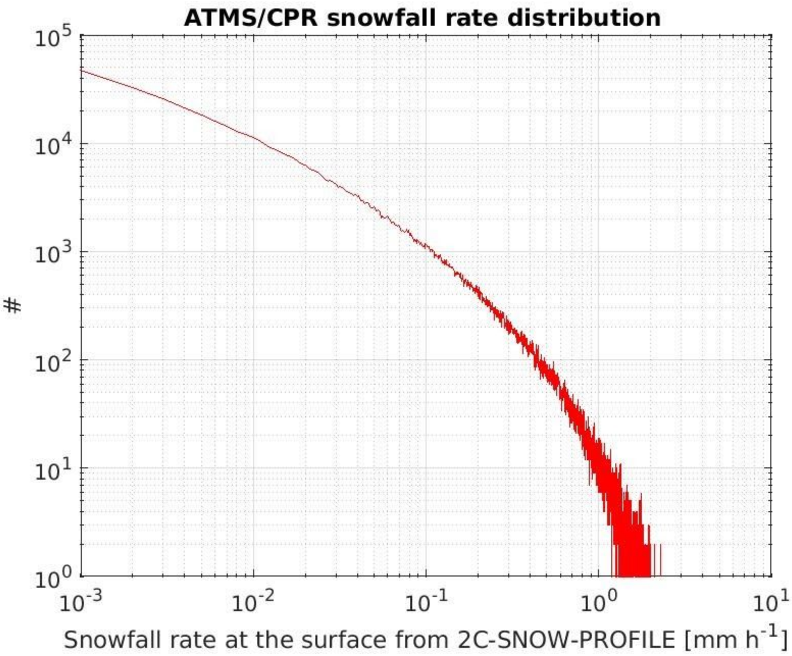

Figure 2.2.2 Snowfall rate distribution in the ATMS/CPR dataset.

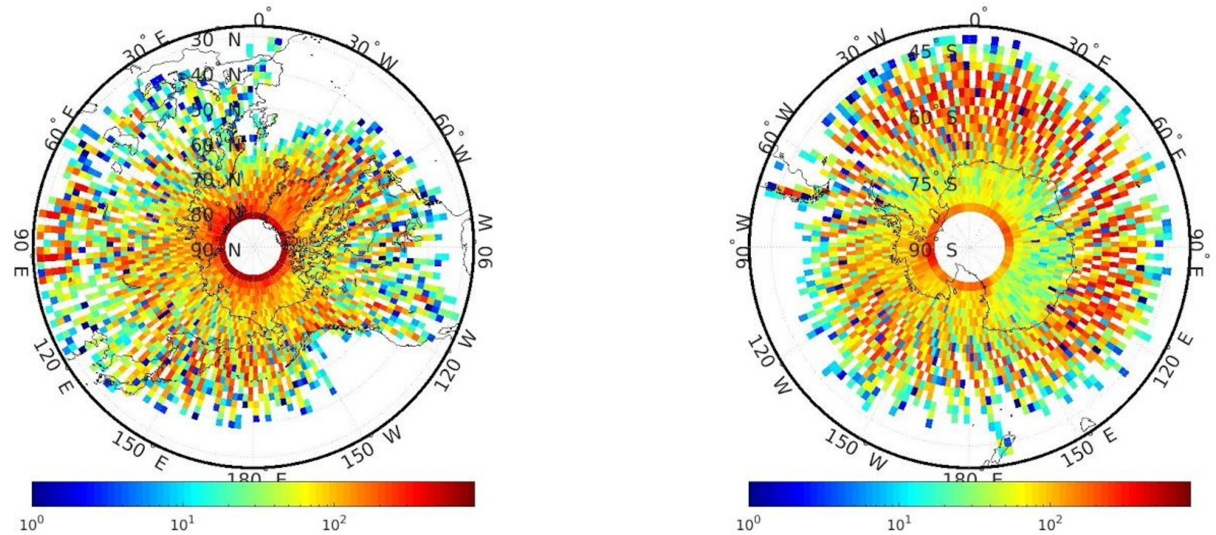

Figure 2.2.3 Map of snowfall occurences in the ATMS-CPR dataset

3. CloudSat-based analysis of GMI and ATMS sensitivity to snowfall

The two datasets built from co-located measurements of CloudSat CPR with the cross-track scanning ATMS and the conically scanning GMI radiometers described in Section 2 have been used to analyse snowfall observational capabilities of the PMW sensors, with particular focus on higher latitudes and cold regions. In this Section 3, an overview of recent studies on GMI and ATMS snowfall observations is provided, followed by the analysis of case studies extracted from the GPM/Cloudsat and ATMS/CloudSat datasets.

3.1 GMI snowfall observation capabilities

3.1.1 Analysis of GMI high-frequency channels and 166 GHz polarization signal

GMI is the first spaceborne radiometer equipped with high frequency (> 100 GHz) dual-polarization channels and, while numerous previous studies have thoroughly studied 183 GHz channels for surface snowfall applications (e.g., Kongoli et al., 2015, Edel et al., 2019), few studies have analyzed high frequency channel polarization sensitivity to snowfall, and these are based on ground-based measurements. The first work on GMI snowfall observation capabilities based on coincident GMI and DPR by You et al. (2016), determine optimal channel combinations for snowfall detection over land. Low frequency channels obviously demonstrate little information due to a weak ice scattering response. Including high-frequency channels near the 183.31 GHz water vapour absorption line ensures valuable information, but adding the 166 GHz channel to a multi-frequency channel combination is deemed optimal for snowfall detection using a GMI-like sensor. The 166 GHz channel amplifies ice/snow scattering sensitivity lower in the atmosphere, yet appropriately suppresses surface influences and increases snowfall detection statistics when compared to radar-derived snow/no-snow statistics. A recent study by Ebtehaj and Kummerow (2017) using GMI and DPR data, illustrates that snowfall detection may be possible over land with no snow cover by using combined 10 and 166 GHz horizontal polarization channel information, while 89 GHz horizontal polarization observations provide crucial information for snow-covered surfaces. Gong and Wu (2017) used the GPM DPR as reference for any information related to the precipitation. They observed that the 89 and 166 GHz polarimetric measurements contain ample information regarding frozen particle habit and orientation. The TB differences (ΔTB) between vertically (V-pol) and horizontally (H-pol) polarized 89 and 166 GHz channel observations are found to be positive, with a distinctive bell-shaped ΔTB curve as a function of V-pol TB that peaks at near 10 K for both channels. The ΔTB values are positive because of stronger H-pol extinction under cloudy conditions that may contain significant columnar liquid water and ice paths. Cold-season high latitude ΔTB-TB relationships are more complex than the generally invariant low latitude ΔTB-TB relationships. This motivated the need to investigate ΔTB-TB relationships at higher latitudes, especially 166 GHz (V-H), using CloudSat observations.

In the work by Panegrossi et al. (2017) for the first time an observational dataset built from matched GPM and CloudSat-CPR snowfall observations (mainly occurring at latitudes between 55° and 65°N) has been used to assess GMI snowfall observation capabilities. The study focuses on higher latitude snowfall systems because most of the GMI-CPR coincidences occur around 60°N/S, and it includes very weak snowfall systems that were not considered in DPR-based studies. The study shows the benefits of the use of observational CloudSat-GPM coincidence datasets in addressing sensitivity assessment and how the high-frequency channel response to surface snowfall (in particular the GMI 166 GHz channels, V and H polarization) is critically affected by environmental conditions (e.g., background surface snow cover conditions over land, sea ice concentration over ocean, water vapour content) and by the presence of supercooled droplets, and how such response depends on cloud vertical structure and snowfall intensity.. In their study, the first version of the global NASA GPM-CloudSat coincidence dataset (2B-CSATGPM, Turk, 2016), combined with DARDAR product derived from CPR and CALIPSO lidar measurements (Delanoë and Hogan 2010) supplying predominant particle phase/microphysics composition or constituent classification (e.g., presence of supercooled water), was used. Note that the snow water path (SWP) derived from the 2C-SNOW-PROFILE (2CSP) product (V04) may be underestimated for weak (Z at the first clutter-free bin level below -15 dBZ) or shallow snowfall events.

The authors demonstrated the sensitivity of the 166 GHz GMI channels, and polarization signal, to snowfall and their great potentials for snowfall detection also at higher latitudes. A regression tree statistical analysis applied to the entire GMI-CloudSat snowfall dataset indicates which variables influence the 166 GHz polarization difference and its relation to snowfall. Critical thresholds of various parameters (sea ice concentration (SIC), TPW, ice water path (IWP)) have been found for optimal snowfall detection capabilities. The 166 GHz ΔTB can identify snowfall events over land and sea when critical thresholds are exceeded for TPW, Sea Ice Concentration (SIC) and DADAR Ice Water Path (IWP). Over land (mostly snow covered) 166 ΔTB can be a useful parameter to identify snowfall mainly for TPW > 3.6 kg m^{-2} for moderate to heavy snowfall amounts (IWP > 0.24 kg m^{-2}). In such conditions its variability is somewhat correlated to the snowfall amount. Over sea, the TPW threshold is higher than over land (TPW ≥ 5.1 kg m^{-2}), i.e. higher water vapour amounts are needed to partly mask the background surface effect on the 166 polarization signal. SIC is another important variable and only for SIC > 57% 166 ΔTB is found to have significant correlation with snowfall.

Figure 3.1.1 shows the distribution and occurrences (2-D histogram) of the snowfall pixels of the whole GMI-CPR dataset in the 166 GHz ΔTB/TB 2-D space. Contours identifying the 90% of occurrences in the snowfall manifolds associated with the different background surfaces (land, open water, sea ice) are also shown. The SIC concentration SIC > 57% has been used to separate sea ice from open water. While 166 ΔTBs are positive, as in Gong and Wu (2017), the distinctive bell-shaped ΔTB curve as a function of V-pol TB (peaking at circa 10 K) is not found. The minimum TBs are rarely found below 200K because of the weak scattering effect by the ice particles associated with snowfall at higher latitudes. Moreover, the behavior of 166 ΔTB versus TB in the upper right portion of the scatterplot (for the whole and open water manifolds) corresponds to what is shown in Gong and Wu (2017) at 89 GHz. The highly polarized signal (high 166 ΔTB values) is due to the large impact of the background surface and to the low opacity of the atmosphere in dry conditions. There is a very distinct behavior of the ΔTB/TB relation for the three different surface types. It is worth noting the different shape and range of 166 ΔTB values of the sea ice manifold with respect to the open water manifold, and its similarity to the land manifold due to the lower polarization found in both cases with respect to open water. The range of TB values at 166 GHz (V-pol, but the same holds for H-pol) for the three manifolds, however, is quite different.

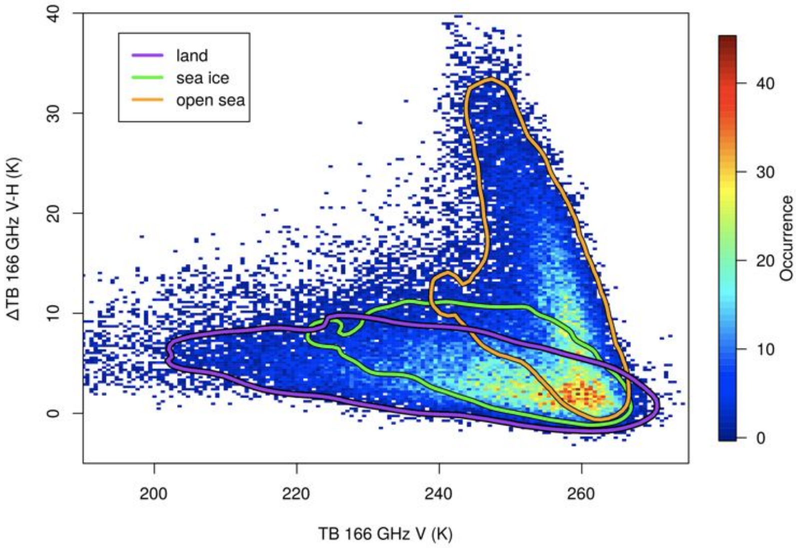

Figure 3.1.1. Scatterplot of the 166 GHz ΔTB/TB 2-D histograms for the whole GMI-CPR snowfall dataset. The 2-D histogram is created by dividing the ΔTB/TB space in 200x100 bins. Each dot represents the mean ΔTB or TB value in each 2D bin while the colorbar indicates the % of occurrences. Contours for 90% snowfall occurrences in the three background surface manifolds are also superimposed: open water (orange), land (purple), sea ice (SIC > 57%) (green) (*from Panegrossi et al., 2017*).

Figure 3.1.2 shows the same distribution of the snowfall pixels as Figure 3.1.1 in the ΔTB/TB 2-D space with mean snow water path (SWP) (as estimated from the CPR 2SC product) and TPW values for each bin indicated by the colorbars, for the different surface types.

Over land we observe that for TPW > 3-4 kg m^{-2}, for any given TB value, ΔTB increases as the SWP increases, showing a good correlation between 166 ΔTB and snowfall. These results confirm that ΔTB can be a valuable parameter for snowfall detection over land when the atmosphere is moist enough to mask the signal from the background (i.e., TPW > 3.5 kg m^{-2}). The same holds for 166 GHz TB (V-pol) > 260K. In this region of the scatter diagram where the bins are characterized by large TPW (TPW > 10 kg m^{-2}) and low SWP values (SWP < 0.01 kg m^{-2}), the water vapour emission reduces the polarization effect and the weak scattering effect due to the snow at 166 GHz. It is also worth noticing that the largest snowfall amounts (SWP > 0.5 kg m^{-2}) are mostly found for 220 K < TB < 260 K.

Over ocean (open water or SIC < 57%) two different regions can be identified. Depending on the snowfall regime the behavior of ΔTB versus TB changes significantly. One region is characterized by a linear relationship between ΔTB and TB for the lower SWP values (SWP < 0.1 kg m^{-2}), with decreasing ΔTB (from 30 K to 0 K), and increasing TB (from 260 K to 270 K) as TPW increases, as expected, and with a slight dependence on SWP. In this region, the ΔTB signal is either dominated by the surface contribution or by the dampening effect on the TB polarization by the water vapour. The other region is characterized by the largest values of SWP (SWP > 0.1 kg m^{-2}) associated with high values of TPW, but also in this case the impact of snowfall on the TB polarization is not significant. Thus, over open water ΔTB is not related to snowfall due to the high polarization induced by the surface. On the other hand, 166 GHz TBs are more correlated with SWP, as the lowest TBs are associated with the highest SWP. Therefore, over open water (or low SIC), TBs at 166 GHz could be used to retrieve snowfall intensity, mostly in presence of intense snowfall events and moist conditions (SWP > 0.5 kg m^{-2}, and TPW > 10 kg m^{-2}).

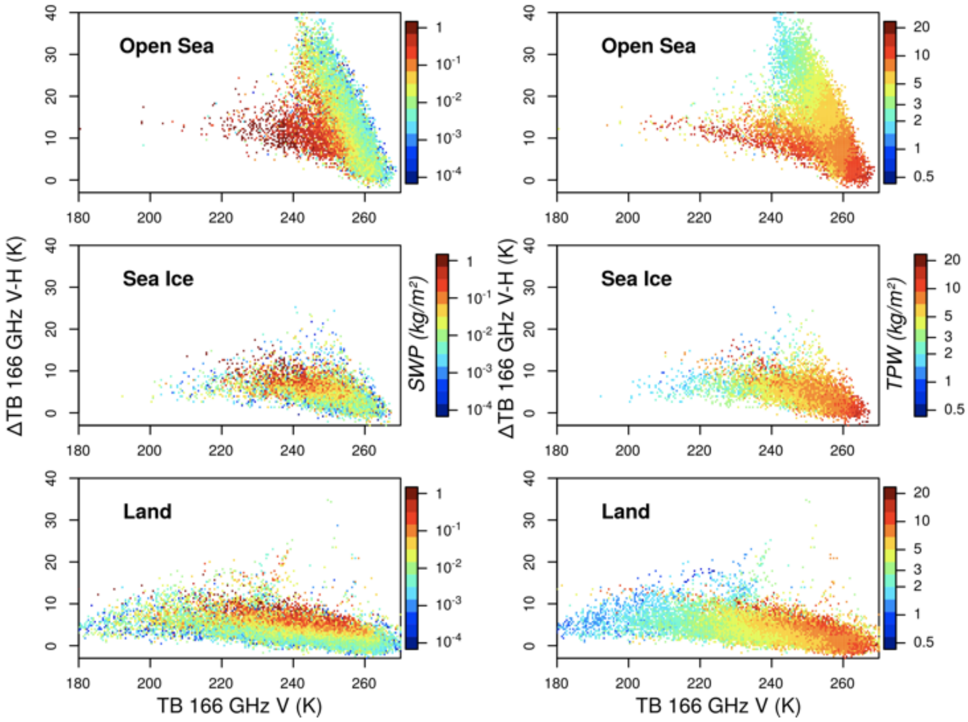

Figure 3.1.2. Scatterplots of the ΔTB/TB for snowfall pixels in the three surface type manifolds: open sea (SIC < 57 %) (top), sea ice (SIC > 57%) (middle row), and land (bottom row). ΔTB/TB space is divided into 200x100 bins, and the mean SWP (left panels) and TPW (right panel) values in each ΔTB and TB bin are represented (in log scale).

<u>*Over sea ice*</u> (SIC > 57%), the almost linear relationship found between ΔTB and TB is similar to the land signature because of the lower impact on the polarization due to the water surface. The ΔTB signal is also related to the SWP (increasing as the SWP increases). TPW has a lower range of values with respect to open water, with TPW mostly < 5 kg m^{-2}.

These results again confirm that 166 ΔTB can be a useful variable for snowfall detection (and retrieval) over sea ice, as well as over land. However, while over land TPW has a much larger range of variability and TBs at 166 GHz (ranging from 170 K to 270 K) do not show a strong relationship with SWP, over sea ice TPW variability is lower, and the TBs show a stronger dependence on SWP, decreasing from 270 K to around 220 K as SWP increases.

3.1.2 Impact of supercooled droplets

Several studies have shown that snowfall scattering signal tends to be masked by the increased atmospheric emissivity and liquid water content in precipitating conditions (Johnson et al., 2016, Liu and Seo 2013, Wang et al. 2013). Previous studies based on ground-based measurements (e.g., Kneifel et al. 2010, Xie et al, 2012) showed that TB enhancement can occur in presence of snowfall, and that high SWP enhances polarization differences at 150 GHz, while the presence of supercooled water reduces the polarization differences. This was also found in more recent studies based on GMI/DPR combined measurements (e.g., Ebtehaj and Kummerow, 2017, Takbiri et al., 2018, 2019).

In the study by Panegrossi et al. (2017), the impact of the presence of supercooled water as inferred from the DARDAR product, on higher-latitude snowfall GMI observation capabilities has been analyzed in detail. The whole GMI-CPR dataset has been divided into four sub-groups: clear sky (CS, which means SWP = 0 kg m^{-2}), snowfall (SN, for SWP > 0 kg m^{-2}, and no supercooled water), snow with supercooled droplets on the top cloud layers (SLCT), and snow with supercooled droplets embedded in the cloud (SCE). Figure 3.1.3 shows the variability of the median 166 ΔTB and 166 GHz (V-pol) TB values vs. TPW values for the different sub-groups. The results are shown for land and sea ice, the conditions where 166 ΔTB responds mostly to the cloud and is less contaminated by the surface.

Over land, median TBs increase with TPW (as expected because of the increasing emission by the water vapour), and in presence of snowfall, and for TPW > 4 kg m^{-2} (close to the TPW threshold found by the regression tree analysis), the median TBs of snowfall cases (SN) are systematically lower compared to clear sky (because of the scattering by the ice). However, the presence of supercooled droplets significantly impacts the TBs, especially when they are found on the top of ice cloud layers (SLCT). In such cases, median TBs can be up to 10 K higher (on average) than snow-only cases. This is due to the emission by the water droplets and also to the fact that, on average for each TPW bin, the SWP found in presence of supercooled droplets (SLCT and SCE) is lower than for snowfall clouds with no supercooled droplets (SN).

Over sea ice (SIC > 57%), a clear distinction of the median 166 GHz TBs versus TPW curves in clear sky (CS) and with snowfall (SN) is visible only for TPW > 4 kg m^{-2}, with median TBs lower for SN than for CS. In such conditions, the effect of the supercooled droplets is to significantly increase the TBs up to values comparable to CS when they are on top of the ice cloud layer (SLCT), and to values between CS and SN when they are embedded in the cloud. In very dry conditions (TPW < 5 kg m^{-2}), the supercooled droplet emission effect on TBs is noticeable. When they are on top of the cloud layer (SLCT), TBs are higher than for CS or for SN. When the supercooled droplets are embedded in the cloud (SCE), the effect of the emission by the droplets is reduced, and median TBs become comparable to CS (or to SN). It is worth noting that over land (top left panel), in very dry conditions, all curves almost overlap to each other, showing no effect of the presence of supercooled droplets on the median TBs. However, as pointed out by Panegrossi et al. (2017), the effects of supercooled droplets on the TBs is clearly visible in such conditions for selected cases (see Section 3.3). In very cold and dry conditions (i.e., and when the emission by the water vapour at 166 GHz is negligible) supercooled droplets on top of the ice cloud layer corresponded to 166 GHz TB increases in presence of snowfall with respect to the clear sky region. In moist conditions such effects are dominated by the water vapour emission.

The lower panels in Figure 3.1.3 show that both over land (for TPW > 5 kg m^{-2}) and over sea ice, snowfall (SN) shows higher ΔTB values than in clear sky (CS) due to the polarization effect by the ice at 166 GHz., in presence of supercooled droplets such effects are reduced, as the emission effect decreases the ice polarization effect. ΔTB median values are correspondingly lower compared to SN, and become comparable to clear-sky conditions when the droplets are found on top of the ice cloud. As pointed out above, this is also due to the fact that for each TPW bin SLCT cases (and to a lesser extent SCE cases) are associated with SWP lower than for SN cases. Panegrossi et al. (2017) also show that 166 ΔTB increases with SWP also in presence of supercooled droplets, meaning that the depolarization effect at 166 GHz induced by the cloud droplets is on average not enough to eliminate completely the polarization effect at 166 GHz by the ice crystals in presence of snowfall. This shows that ΔTB can be a very valuable parameter to use for snowfall detection and quantification for the following difficult circumstances: (1) over snow-covered land, (2) for very weak snowfall events (very low SWP), and (3) for low TPW values in 4-5 kg m^{-2} range.

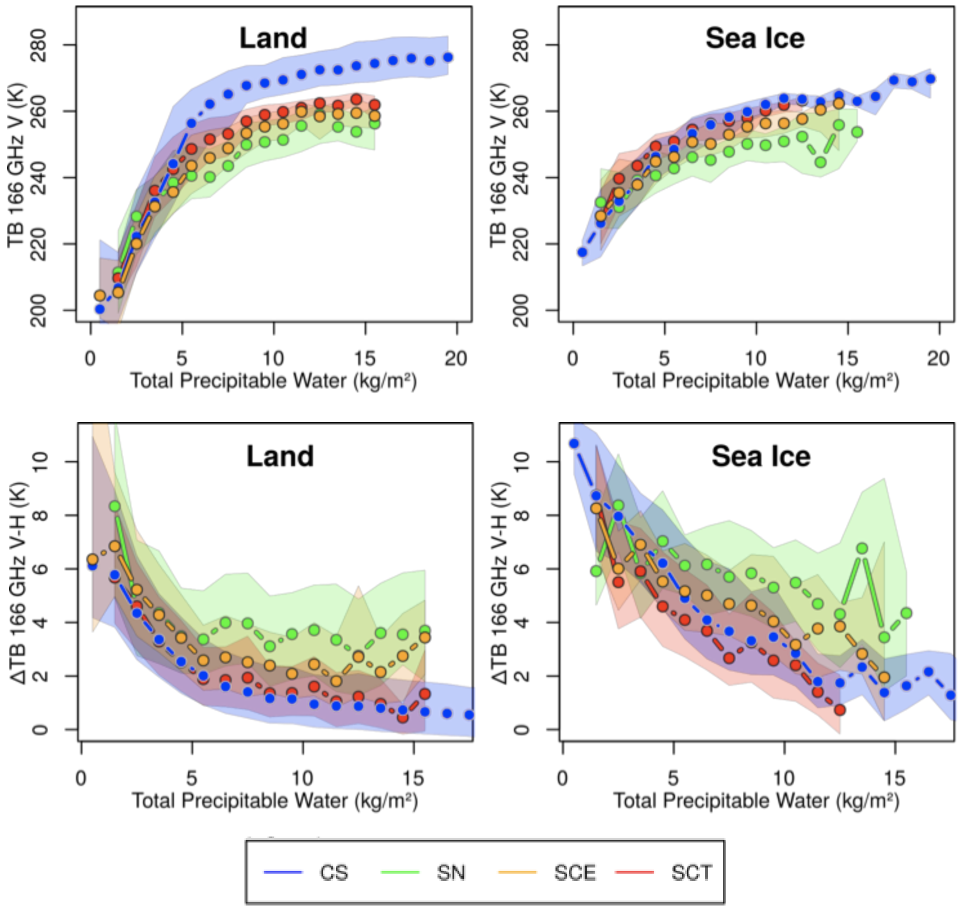

Figure 3.1.3. Median values of TBs at 166 GHz (V-Pol) (computed in TPW and SWP bins) as functions of TPW (top panels) and SWP (bottom panels) for clear sky (CS, blue), snow (SN, green), snow + embedded layer of supercooled (SCE, orange), snow+ supercooled layer on top (SLCT, red). The colored shades represent the spread of the TBs between the 25th and 75th percentiles in each manifold. The dataset has been divided into 21 TPW bins (top panels) and 11 SWP bins (bottom panels), and only the results for bins with at least 20 pixels are shown (for statistical significance). Sea ice results are shown for SIC > 57%. In the bottom panels the results are shown for TPW > 3.6 kg m^{-2} over land, and for TPW > 5.1 kg m^{-2} over sea ice (from Panegrossi et al., 2017).

A very striking example of GMI snowfall observation capabilities also in extreme conditions has been provided by a recent study by Milani et al. (2020) who analyzed GMI measurements of intense *lake-effect snow bands* over the lower US Great Lakes region. Lake-effect snow is a form of shallow convective snow produced during cold-air outbreaks, whereby cold air interacts with unfrozen or partially frozen bodies of water. This snowfall mode commonly occurs in the United States Great Lakes region. Spaceborne radar datasets also highlight its prevalence globally with distinct seasonal cycles and notable shallow convective maxima located over extended high-latitude oceanic regions (Kulie and Milani 2018; Kulie et al. 2016). To globally assess water resources, it is particularly important to detect and retrieve shallow convective snowfall. Surface temperatures and columnar water vapour levels associated with lake-effect snow are usually very low (e.g., < 5 kg m^{-2}), with low water vapour amounts portending potential PMW detection difficulties. Figure 3.1.4 shows the high-frequency GMI channel response to a Lake-effect snow event occurred on 20-21 November 2014 over Lakes Erie and Ontario (T2m ranged between ~263 and 274 K during the event, and TPW values between 4-5 kg $^{m-2}$).

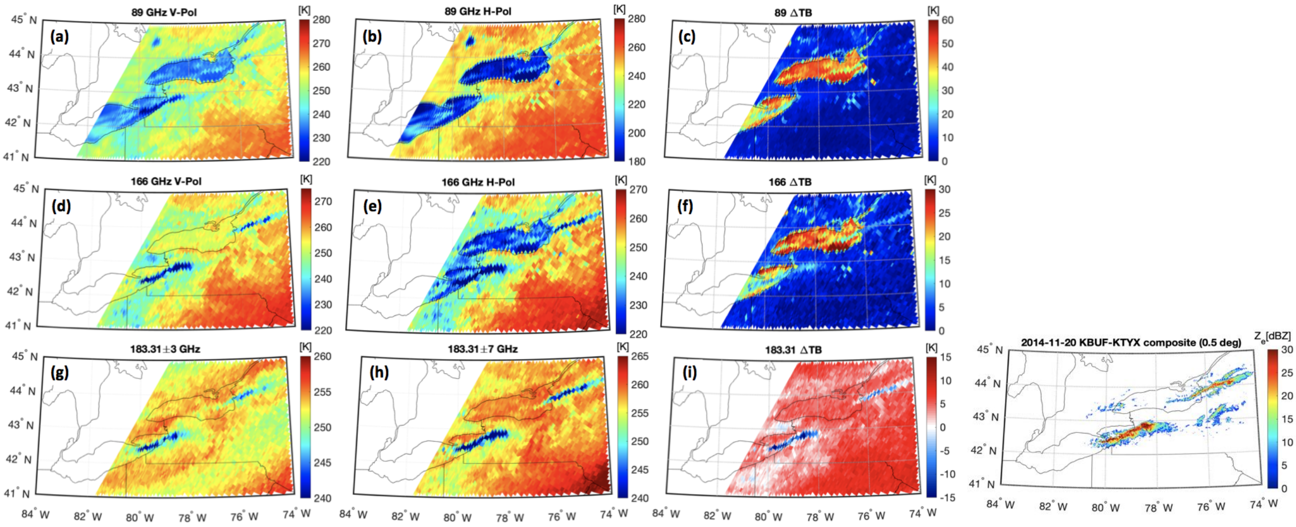

Figure 3.1.4. GMI (a) 89 GHz vertical (V) polarization BT [K], (b) 89 GHz horizontal (H) polarization TB [K], and (c) 89V-H TB differences [K] for 1820 UTC 20 November 2014 (GPM orbit #4140). GMI (d) 166V, (e) 166H, (f) 166 V-H, (g) 183.3±3, (h) 183.3±7, and (i) 183.3±7 - 183.3±3 TB differences are also shown. Right Panel: NEXRAD base scan composite radar reflectivity using the Buffalo (KBUF) and Fort Drum (KTYX) sites at 1818 and 1821 UTC 20 November 2014. (*from Milani et al., 2020*f)

All window channels highlight large land surface emissivity variability, with higher TBs in the sparsely snow-covered/vegetated southeastern portion of the domain, and lower TBs in presence of deep-dry snow around the lakes. TB emission signals are found in *89 and 166 GHz* channels over the lakes (a-f) due to cloud water emission. GMI higher frequency (89-183.31GHz) channels can also delineate likely surface snowfall regions since they are progressively more sensitive to frozen hydrometeor scattering signals. As a result, over the eastern lake surfaces, warmer TBs from likely cloud water emission at 89 and 166 GHz evolve into distinct TB depressions as cloud thickness, snow/ice particle size, integrated columnar ice paths, and surface snowfall rates increase . The snow band observed by NEXRAD over eastern Lake Erie (79.5W-77.5W) and extending inland for almost 100 km is accompanied by GMI 166 GHz TB depressions reaching ~30K (d,e). Lower TB depressions are also apparent at 89 GHz. Polarization difference signatures are also noteworthy over land in the Lake Erie snow band. Similar 89 and 166 GHz signals, albeit with lower TB depression magnitudes, are also evident in the NEXRAD-observed Lake Ontario snow band (77W-74W).

The 183.3±7V and 183.3±3V GHz channels provide further evidence that distinct GMI signals accompany this lake-effect snow event. These channels offer increased ice/snow particle scattering sensitivity, but their respective locations near the 183 GHz water vapour absorption line typically provide information from mid- to upper-atmospheric levels and therefore might not be deemed appropriate for shallow precipitation remote sensing applications. However, very low TPW values allow 183 GHz weighting functions to peak at lower atmospheric levels and therefore respond to the lake-effect snow bands (e.g., Edel et al. 2019). $TB_{183.3±7}$ and $TB_{183.3±3}$ differences (ΔTB_{183}) effectively isolate the lake-effect snow bands, with ΔTB_{183} values below -15K in the most intense snowfall locations (i). Furthermore, ΔTB_{183} signals over land are much more distinctive than ΔTB_{89} (c) and ΔTB_{166} (f). The Lake Erie snow band is inferred to be more intense than the Lake Ontario snow band due to larger ΔTB_{183} magnitudes.

3.1.3 Impact of background surface conditions: effects of snow cover

Several studies evidence how critical is the correct characterization of the environmental conditions (frozen background surface conditions, water vapour and cloud liquid water content, near surface temperature) for snowfall detection and retrieval from PMW radiometer observations.

Takbiri et al. (2018) consider the combined effect of snow-cover depth and cloud liquid water content on microwave signatures of terrestrial snowfall using multi-year observations by GMI and reanalysis data, with particular emphasis on 89 and 166 GHz channels. Falling snow weakens its radiometric signatures in microwave bands when it begins to accumulate on the ground. It is found that over the shallow snow cover depth (< 10 cm) and low values of cloud liquid water path (LWP < 70 gm^{-2}), the light snowfall (< 1 mmh^{-1}) scattering is detectable only at frequency 166 GHz while for higher intensities the signal can be also detected in 89 GHz. However, when snow depth exceeds 20 cm and the LWP is greater than 70 gm^{-2}, the emission from the increased liquid water content in snowing clouds becomes the only snowfall signature, stronger at 89 GHz than 166 GHz. The results also reveal that over high latitudes above 60° N where the snow cover is thicker than 20 cm and LWP is lower than 70 gm^{-2} , the high-frequency channels (> 166 GHz) are totally blind to snowfall below 0.5 mmh^{-1}. This is because of the stronger response of the 89 GHz to the background scattering compared with that of 166 GHz, resulting in a large decrease in the surface emissivity when snow starts to accumulate on the ground, making the surface radiometrically much colder at 89 GHz than at 166 GHz.

Takbiri et al. (2019) further analyzed GMI multi-channel response to snowfall compared to rainfall (using DPR precipitation profiles) in presence of different land surface conditions (*vegetated land, wet (shallow) snow, dry (deep) snow*). They demonstrate that the snowfall signal exhibits a weaker scattering signal than rainfall and reveal that there exists a non-unique relationship between the brightness temperatures and snowfall rate over snow-covered surfaces. For snowfall over the surfaces with no snow cover, as a result of the snowfall scattering, the average brightness temperature at the 166-GHz frequency channel decreases about 14–20 K, which corresponds to a cooling of 1.75–2.50 K per unit snowfall rate. This observation reaffirms the importance of 166 GHz for snowfall retrieval compared to the 89-GHz channel (see Bennartz and Bauer 2003, Skofronick-Jackson et al. 2013, You et al. 2017, Panegrossi et al., 2017). When snow begins to accumulate on the ground, the snowfall scattering signal decreases at frequencies > 89 GHz. Takbiri et al. (2019) evidence the interesting non-monotonic response of the observed brightness temperatures to the snowfall rate over snow-covered surfaces. For example, over the dry snow, the brightness temperatures at >89 GHz increase when the snowfall intensity varies from 2 to 4 mm h^{-1} , showing an irregular transition from a scattering to an emission regime. The possible reasons for this anomaly could be related to an emission signal from either the atmosphere or the land surface. The atmospheric-related reasons can be due to the enhanced emission from the cloud liquid water and/or the water vapour path; both of them often increase with increasing snowfall intensity (Liu and Seo 2013; You et al. 2017; Ebtehaj and Kummerow 2017). The land-surface-related causes largely correspond to the increased surface temperature and/or changes in the snow-cover physical properties. Takbiri et al. (2019) demonstrate that the anomaly is largely due to changes of the surface conditions and snow cover dynamics, and that GPM-based light but prolonged snowfall intensities (< 2 mm h^{-1}) occur at latitudes above 58°N over dry and thicker snow cover. High-intensity but less-frequent snowfall (based on DPR) more likely occurs over lower latitudes with a thinner snow-cover climatology. In other words, the high snowfall rates mostly represent the climatology of lower latitudes with thinner depth of snow cover, less volume scattering, and thus stronger surface emission than the thicker snow cover of higher latitudes. When the snow-cover scattering increases, the precipitation signal transitions from a scattering to an emission regime. The wet snow cover weakens the precipitation scattering as it is less emissive than the ground with no snow cover. However, the less emissive dry snow reveals the precipitation emission signal. Figure 3.1.5 (from Takbiri et al., 2019) clearly evidences the different multi-channel response of GMI to the presence of snowfall for different surface conditions.

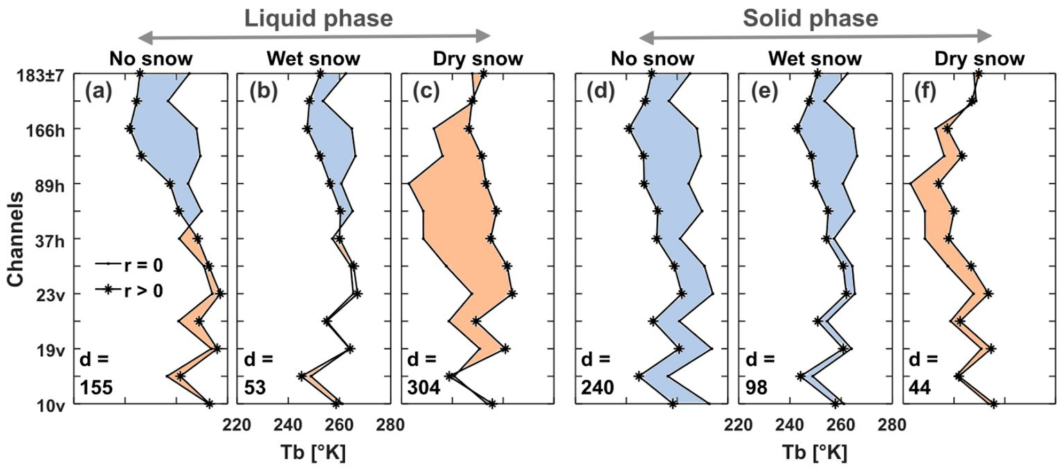

Figure 3.1.5. Average distance between vectors of mean brightness temperatures in the database from June 2014 to May 2016 for a clear sky (r = 0) and a near-surface precipitating atmosphere (r > 0) with (a)–(c) liquid and (d)–(f) solid phase precipitation over land with no snow cover, wet snow cover, and dry snow cover. The blue and orange shaded areas indicate the cooling (scattering) and warming (emission) signals of precipitation. The mean root squared distance between the no precipitating (clear sky) and precipitating atmosphere is also presented for each land–atmosphere class (*from Takbiri et al., 2019*).

Over the wet snow cover, the dominant rainfall signal is due to its scattering over high-frequency channels, although less evident than over vegetated land. However, when the surface emission is significantly reduced over the dry snow, the emission of rainfall can be detected as a warming signal across almost all frequency channels. For the solid phase, the distance is relatively large between the background and precipitation signals when there is no snow on the ground. Similar to the liquid precipitation, this distance shrinks when the ground is covered with wet snow, where the shift between the background temperatures almost vanishes as the surface temperature increases. When the snowfall is occurring over dry snow, an emission signal is observed, chiefly in response to the increased liquid and water vapour paths (see Liu and Seo 2013; You et al. 2015, 2016; Ebtehaj and Kummerow 2017, Panegrossi et al., 2017). This emission signal (which causes a TB warming compared to the clear sky touchstone) indirectly indicates the likelihood of precipitation and could be used to improve snowfall retrievals over dry snow cover (as in Takbiri et al., 2019).
All these studies evidence how it is fundamental to be able to characterize the frozen background surface at the time of the overpass. One way to do this is by exploiting the information of the low-frequency channels (less affected by the atmospheric and cloud contribution in presence of snowfall). This topic is analysed in detail in Section 5.

3.1.4 GPROF and SLALOM snowfall retrieval algorithms for GMI

GMI-based snowfall retrieval has recently seen great interest and efforts, mainly motivated by the need of fully exploiting the capabilities of this radiometer, illustrated in the previous sections, and in preparation for future operational space missions (e.g., EPS-SG MWI). In this study we focus on two retrieval algorithms: one is the operational NASA GPM PMW radiometer algorithm and one is a newly developed CloudSat-based algorithm for GMI developed at CNR-ISAC within the EUMETSAT H SAF program (Mugnai et al., 2013, *http://hsaf.meteoam.it*).

The **Goddard PROFiling algorithm** (GPROF, Kummerow et al., 1996, 2001, 2011, 2015) is the NASA operational precipitation retrieval algorithm for the GPM PMW constellation radiometers (including GMI) and its output solution is a cloud and precipitation profile derived from a predefined database of possible solutions (referred as an *a-priori* database). A *Bayeasian* inversion formulation is used to find the output profile which is the most radiometrically consistent with the set of multi-frequency measured brightness temperatures. Details on the Bayesian theory can be found in Rodgers (2000), while further details about GPROF's evolution are presented in Kummerow et al., 2011, 2015). In order to limit the search only to appropriate cloud regimes, the a-priori database is partitioned using various ancillary data: T2m, TPW, and surface type with the goal of separating surfaces with similar microwave emissivity. Surface types are obtained from a SSM/I-observed emissivity climatology (Aires et al. 2011) and its daily updates by NOAA's AutoSnow product (Romanov et al. 2000). The TPW and T2m parameters are obtained from the Global Atmospheric Analysis (GANAL; JMA 2000) and the European Center for Medium-Range Weather Forecasts (Dee et al. 2011) reanalysis data sets for the operational (GPROF) and the climatological GPROF (GPROF-CLIM) outputs, respectively.

In the GPROF version 5 (V5) for GMI used in this study the *a-priori* database relies on DPR Ku precipitation retrievals (V04) over vegetated surfaces, inland waters and coastlines and on the DPR-combined (CMB V04) algorithm (Grecu et al. 2004, 2016) over oceans, sea-ice and sea-ice/ocean boundaries. The database is built with one year of GPM data (DPR and CMB), from September 2014 to August 2015. Ground-based Multi radar Multi sensor (MRMS) system (Section 4) precipitation estimates from the polarimetric NEXt generation weather RADars (NEXRAD) and automated rain gauge networks in the CONterminous US (CONUS) and southern Canada (Zhang et al. 2011, 2016) are used over snow-covered surfaces. The database is built matching two years of MRMS data (from April 2014 to August 2016) with satellite overpasses. This implies that over snow covered land surfaces, the GPROF retrieved solution is expected to closely approximate the MRMS observations. The precipitation phase is determined following the methodology proposed by Sims and Liu (2015) for all surface types, including snow-covered surfaces, in order to have a common classification method with the other two *a-priori* databases (DPR- and CMB-based) (ATBD GPROF2017 Version 1).

Studies dedicated to the quality assessment of GPROF V05 snowfall rate estimates have evidenced the good ability of GPROF to detect more intense frontal snowfall events, and a clear dependence of GPROF detection skill on cloud echo top height, with a scarce ability to detect shallow snowfall events (von Lerber et al., 2017). The authors report a *general underestimation* of GPROF by a factor 3 to 6 for 26 cases compared to high-quality ground-based radar measurements over Finland. Milani et al. (2020) have analysed the GPROF capabilities for intense lake-effect snow events over the lower U.S. Great Lakes region, comparing it to MRMS snowfall rate product. In spite of GMI sensitivity to these kind of snowfall systems (Figure 3.1.4), they found that GPROF *misses and/or underestimates intense (and shallow) lake-effect snowfall*, while it tends to provide *very light snowfall* where the ground-based radar does not see precipitation (Figure 3.1.6). The authors have attributed this to the poor representativeness for these types of snowfall events in the GPROF a-priori database, and to the snow-covered surface characterization, especially along the coast of the lakes interested by the heaviest snowfall. An *a-priori* database sensitivity test has been carried out by forcing GPROF to use the MRMS-only *a-priori* database over all surface types (including coast lines), and filtering the results with a minimum snowfall rate threshold (around 0.1 mm h^{-1}), and demonstrated significant GPROF detection and QPE performance improvements (Figure 3.1.6). Further evidence of the GPROF shallow convective snowfall detection limitations, has been provided in the work by Skofronick-Jackson et al. (2019). Figure 3.1.7 shows the global maps of three year (2014-2017) snowfall occurrence percentage obtained from the CloudSatCPR 2CSP and from GPROF-CLIM products from Skofronick-Jackson et al. (2019). The maps reveal the tendency of GPROF to miss precipitation in regions where CPR 2CSP shallow (convective) snowfall likely occurs (e.g., northern Atlantic Ocean, the Labrador Sea) (Kulie et al., 2016).

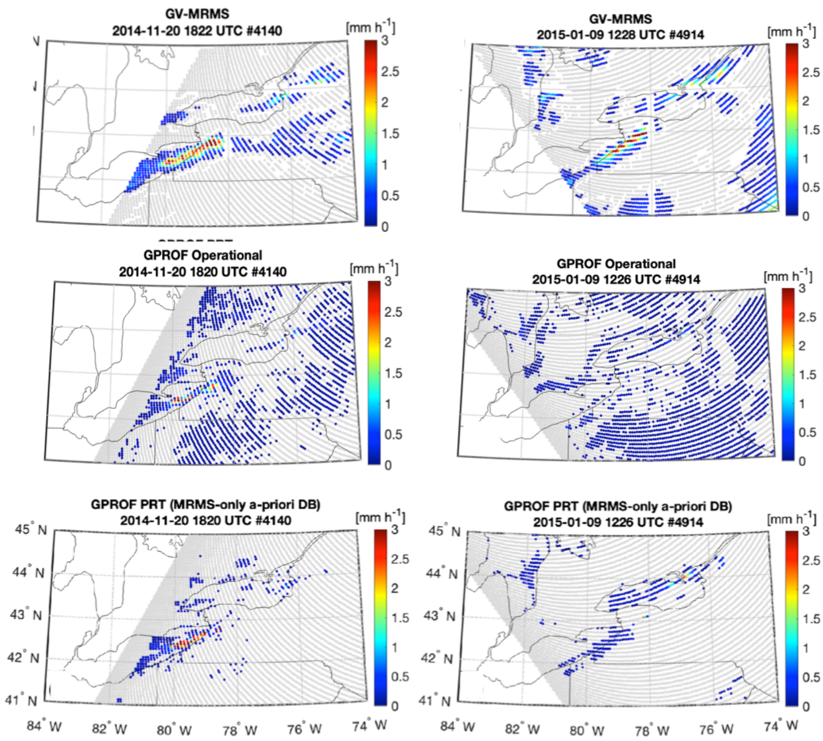

Figure 3.1.6: GPROF results for Lake effect snow cases over the U.S: Great Lakes region. MRMS-GV snowfall rate (top panels), operational GPROF precipitation rate (middle panel) and GPROF precipitation rate with minimum threshold ~0.1 mm h^{-1} forced to use MRMS-only a priori database over all surface types (*from Milani et al., 2020*)

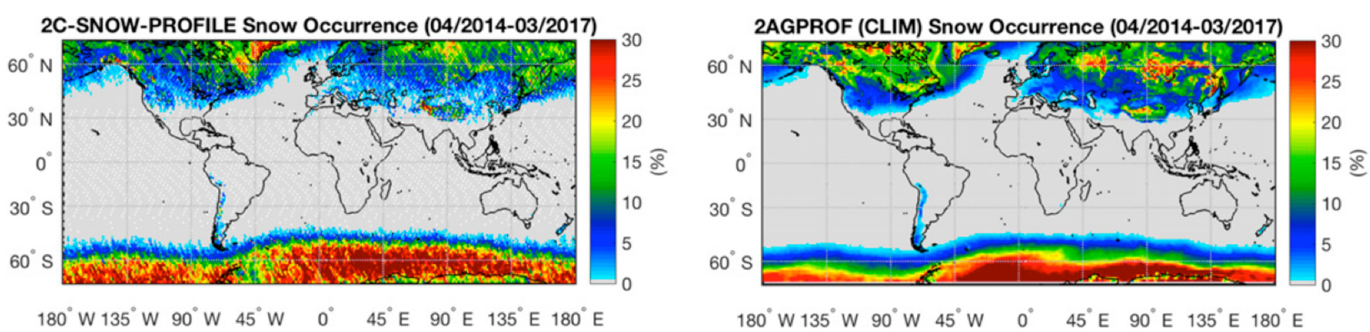

Figure 3.1.7 Global maps of surface snowfall occurrence probability (%) from the CPR 2CSP product and from GPROF-CLIM (V05) (*from Skofronick-Jackson et al., 2019*).

The **Snow retrievaL ALgorithm fOr gMi** (**SLALOM**, Rysman et al., 2018, 2019) is a snowfall retrieval algorithm for GMI based on a machine learning approach, that, in principle, can be extended to other PMW radiometers (such as the EPS-SG MWI). A GMI/CloudSat coincidence database is used for training, where CPR 2C-SNOW-PROFILE (2CSP) snow water path (SWP) and surface snowfall rate (SSR) products are used as reference. The algorithm makes use also of the DARDAR cloud classification product for the detection of supercooled water droplets at the cloud top (SLCT), and of ancillary variables (e.g., ERA-Interim T2m, TPW, humidity profiles). The use of CloudSat-based observational databases makes it particularly tailored to detect and retrieve light snowfall at higher latitudes. The SLALOM algorithm is composed of four modules for (i) snowfall detection, (ii) supercooled droplet detection, (iii) SWP estimation, and (iv) the recently-added surface snowfall rate (SSR) estimation module (Rysman et al., 2019). Snowfall and supercooled detection modules rely mainly on the random forest approach (Breiman, 2001), while the SWP retrieval module uses a segmented multi-linear regression approach (Liu et al., 1997), and the SSR module a gradient boosting method (Chen and Guestrin, 2016). Through the exploitation of all 13 GMI channels and the optimal use of ancillary variables describing the atmospheric conditions (and no ancillary information on the background surface conditions), SLALOM is able to predict snowfall occurrence, SWP, and SSR in good agreement with the Cloudsat 2CSP product, with the advantage of ensuring the much larger spatial coverage provided by the GMI swath. Rysman et al. (2018) report that SLALOM is able to reproduce quite accurately CPR snowfall patterns, with POD of 0.83, with a FAR of 0.12 and a HSS of 0.84 when compared to an independent CPR-based dataset. The SLCT detection module shows a POD of 0.97, with a FAR of 0.05 and a HSS of 0.89, with no significant variability among different surface types. Comparison of SLALOM SWP with CPR SWP estimates provide correlation coefficient of 0.86, e mean relative bias of -20%, and a RMSE of 0.04 kg m^{-2}. The SSR module (Rysman et al., 2019), is able to retrieve surface snowfall rate with a mean relative bias of -13%, a correlation coefficient of 0.7 and a RMSE of 0.08 mm h^{-1} compared to CloudSat observations. However, Rysman et al. (2019) report SLALOM tends to overestimate SSR < 0.05 mm h^{-1} (due to the known limitation of GMI sensitivity to very light snowfall in certain conditions) and underestimate SSR > than 1.5 mm h^{-1} (see Figure 3.1.8). This is due to the scarce representativeness of intense snowfall events in the 2B-CSATGPM coincidence database [only 314 cases over 56,380 snowfall cases with SSR > 1.5 mm.h^{-1} (i.e., see Figure 6 in Casella et al. (2017) for the 2014-2015 period]. Overall, SLALOM SWP retrievals are in better agreement with the 2CSP than the SSR. This confirms that the GMI brightness temperatures respond mostly to the vertical distribution of ice (or liquid) hydrometeors within the cloud while the surface snowfall rate retrieval is quite an indirect estimate that can be derived mostly through statistically-based (or physically-based) approaches that are able to infer relationships between the upper cloud layers and the SSR.

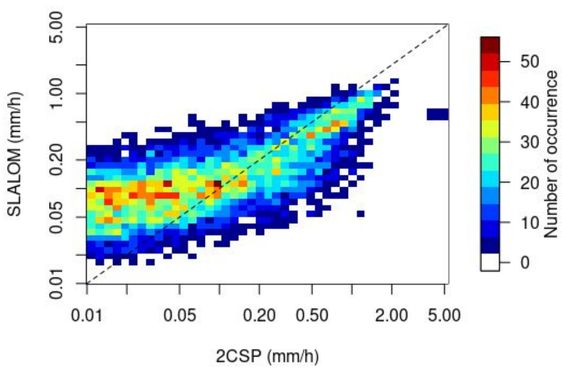

Figure 3.1.8: 2-D histogram of three year (May 2014-May 2017) analysis of SLALOM vs. 2CSP surface snowfall rate.

Figure 3.1.9 shows the global snowfall probability maps obtained from SLALOM and from CPR 2CSP product. The Antarctica coast is the region with the highest occurrence of snowfall, with values reaching 40% in some areas. It is interesting to note the steep decrease of snow occurrence as one moves away from Antarctica. In the Northern Hemisphere, the situation is more complex due to the presence of continents. The maximum is found over Greenland, with values over 40% and values of about 30% in the Labrador Sea. Siberia, Canada and the eastern side of continents show an occurrence between 2 and 20%. Europe and the western side of continents have a snow occurrence lower than 5%. Finally, mountain ranges, such as the Himalayas, the Andes, the Alps and the Rocky Mountains show occurrences that can exceed 20%. These patterns match very well those identified by CPR. Figure 3.1.10 (right panel) shows significant average SSR values in the Southern Ocean region reaching 3.5 mm d^{-1} in its eastern part. In the northern hemisphere, coastal regions of North America and Greenland show local maxima higher than 2 mm d^{-1}. Labrador Sea, western Siberia and Okhotsk Sea (along the Kamchatka Peninsula) also presents a high average snowfall rate. Finally, heavy snowfall rates are found in most mountainous regions (the Himalayas with local maxima above 3.5 mm d^{-1}, the Andes, the Alps and the Rocky Mountains). Those patterns are globally similar to those found in Behrangi et al. (2016), Kulie et al. (2016) although some inconsistencies in some areas are visible.

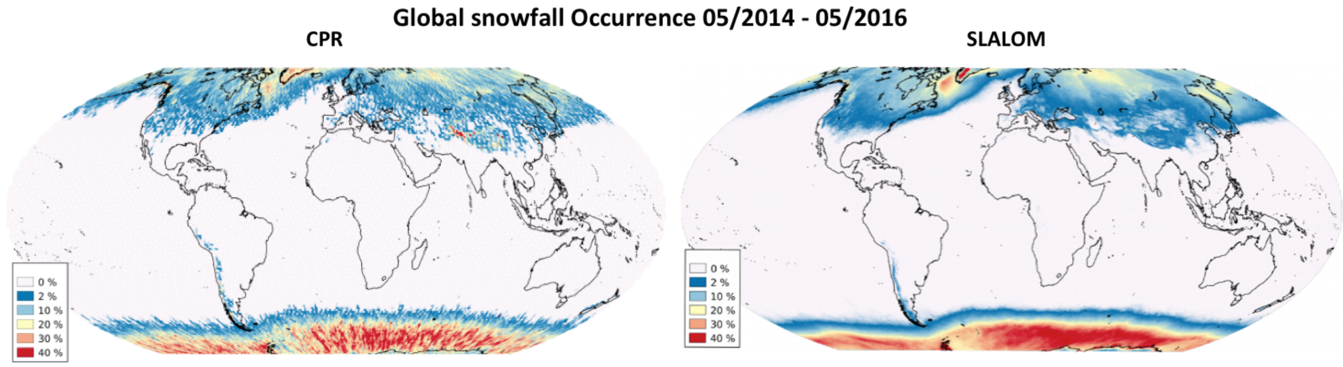

Figure 3.1.9: Top panels: Global maps of snowfall percentage of occurrence obtained from CPR 2CSP product (left) and from the SLALOM snowfall detection module (right), from May 2014 to May 2016 on a 0.1°x 0.1° grid (*from Rysman et al., 2018*).

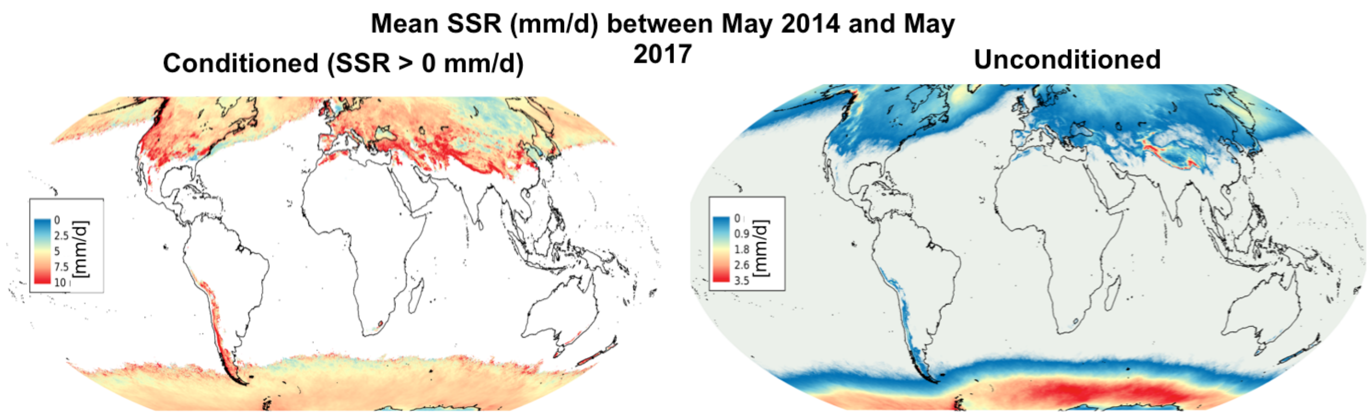

Figure 3.1.10: Conditioned (i.e., for SSR> 0 mm d^{-1}) (left) and unconditioned (right) average surface snowfall rate (mm d^{-1}), as estimated by the SLALOM SSR module from May 2014 through May 2017 (*from Rysman et al., 2019*)

SLALOM is able to reproduce quite accurately CloudSat CPR 2CSP snowfall climatology. However, it is worth mentioning its main limitations that can be summarized as follows:

- it fully relies on the 2C-SNOW-PROFILE CPR product (V04), therefore it tends to miss very shallow snowfall, it only retrieves frozen precipitation (no mixed-phase clouds), and it tends to underestimate moderate-heavy snowfall events;
- the training dataset, based on GMI/CPR coincident observations (mostly concentrated around 60°N/S, see Figure 2.1.3), is mostly representative of higher latitudes snowfall systems, and is affected by the sun-synchronous CloudSat overpassing time (further restricted by its daylight-only operation mode);
- the supercooled detection module only accounts for water droplets at the cloud top, therefore it does not consider the potential effect of embedded supercooled droplets (30% of GPM/Cloudsat snowfall cases).

Some case studies with application of the SLALOM and GPROF algorithms, and comparison with CPR, will be shown in Section 3.3, while Section 4 will provide the results of a validation experiment of GPROF and SLALOM snowfall estimates over the U.S./Canada.

3.2 ATMS snowfall observation capabilities

3.2.1 Review of ATMS recent studies and algorithms

The heritage of the ATMS snowfall retrieval starts when the first operational suite of algorithms for hydrological applications originally developed for the SSMI instrument (Ferraro, 1997) were calibrated for the AMSU channels in order to derive several hydrological parameters (Grody et al, 2000). Staelin and Chen (2000) and Chen and Staelin (2003) were the first to develop a global method for retrieving precipitating system combining the AMSU-A O_2 channel at 53.6 GHz and the AMSU-B/MHS water vapour absorption channels around the band at 183.31 GHz. These pioneering works opened the way to a series of theoretical studies and applications that involved the entire scientific community (Boukabara et al., 2013).
Kongoli et al. (2003) introduced a new snowfall detection algorithm over land. The new scheme combined the AMSU channels in the atmospheric window (23, 31, 89, 150 GHz), opaque water vapour (183.31 ± 1, ±3, ±7 GHz), and oxygen absorption (50–60 GHz) regions for discriminating the scattering features over land surfaces such as snow cover and that of the precipitation-sized ice particles. The sensitivity of the AMSU frequencies were simulated in Skofronick-Jackson et al. (2004) to derive a physical model of radiation at millimeter-wave frequencies seeking to infer snowfall rates over land by taking advantage of water vapour screening to obscure the underlying snow-covered surface. The same case study used for testing the physical model was also exploited to investigate the potentialities of a new AMSU-B-based prototype method (183-SFR) developed by Laviola et al. (2010) and improved in Laviola et al. (2015). The 183-SFR is the combination of three cascade algorithms: the first algorithm based on the AMSU-B TBs calibrated through the NEXRAD radar network measurements over CONUS, screens all potential snowfall clouds. These possible snowy clouds are further analyzed by a second-level algorithm thought for reducing surface contaminations identifying the presence of snow cover (183-SCM). Hence, the snowfall rate is computed with the 183-WSL algorithm (Laviola and Levizzani, 2011; Laviola et al., 2013).
Recently, the 183-SFR was upgraded by a fourth-level analysis exploiting an independent method developed for classifying the cloud type by distinguishing between stratiform and convective clouds. The MicroWave Cloud Classification method (MWCC) originally developed for AMSU-B/MHS (Laviola and Levizzani, 2009; Levizzani et al., 2010; Laviola et al., 2020) and now adapted to the ATMS and to the Imager/Sounder SSMIS, exploits the properties of the high

frequency channels to classify the cloud type (stratiform/convective) by estimating the cloud top altitude and the phase of hydrometeors. The support of the MWCC to the prototype algorithm for snowfall retrieval mitigates the major limitations of the original scheme in detecting light or moderate snowfall in colder weather conditions or frozen soil. In these situations, the brightness temperatures are higher under snowfall than no snowfall conditions, likely due to emission by cloud liquid water. Thus, the brightness temperature increase masks the scattering signal and complicates the retrieval of snowfall (Liu and Seo, 2013). On the contrary, the scattering signal from frozen terrains often dominates the signal from snowy clouds to the satellite. These main problems are discussed in Kongoli et al (2015) where the main algorithm design for snowfall retrieval developed for AMSU-B was fitted for ATMS channels for detecting snowfall over land. The detection technique based on the ATMS high-frequency channels, is trained with ground measurements over U.S. and Alaska during two winter seasons. The algorithm computes the probability of snowfall using logistic regression and the principal components of the seven higher frequency ATMS channels at 89 GHz and above as independent variables. In addition, ATMS channel 6 is used as a temperature proxy to define the snowfall retrieval domain. The snowfall detection algorithm has been applied at NOAA since February 2014 for routine monitoring and evaluation and as snowfall mask for an ATMS-based NOAA SFR algorithm. The SFR retrieval is based on a 1D-Var inversion method and a two-stream radiative transfer forward model (Yan et al., 2008). A method developed by Heymsfield and Westbrook (2010) is adopted to calculate snow particle terminal velocity, which in combination with the retrieved cloud properties of particle size and ice water path (Yan et al., 2008) are used to estimate Snowfall Rate (SFR). An example is provided in Figure 3.2.1 where the sequence of ATMS-retrieved snowfall images over U. S. CONUS describes the significant high-impact storm event that brought heavy rain, ice, and snow over eastern U.S. during 12–14 February 2014.

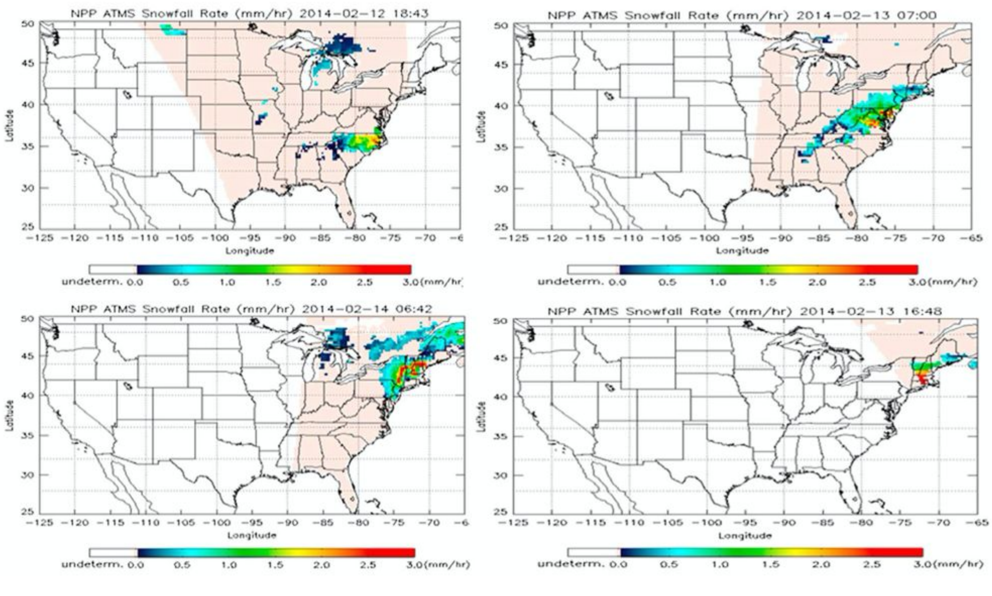

Figure 3.2.1: ATMS-retrieved snowfall images over CONUS U.S. during the severe snowstorm over eastern U.S. during 12–14 February 2014 (*from Kongoli et al., 2015*).

More recent studies have strongly improved previous ATMS retrieval schemes for snowfall by introducing more stringent conditions in the statistics of TBs calibration or employing new designs to enhance the physically-based retrieval of snowfall rates.

The first approach is tracked by You et al. (2016); here the ATMS measurements are interpreted by the linear discriminant analysis (LDA) and Bayesian method described in You et al. (2015) and supported by five ancillary datasets, including surface type data, MERRA data, GPCC monthly precipitation data, and hourly surface gauge observations. An example of the algorithm performance is displayed in Figure 3.2.2.

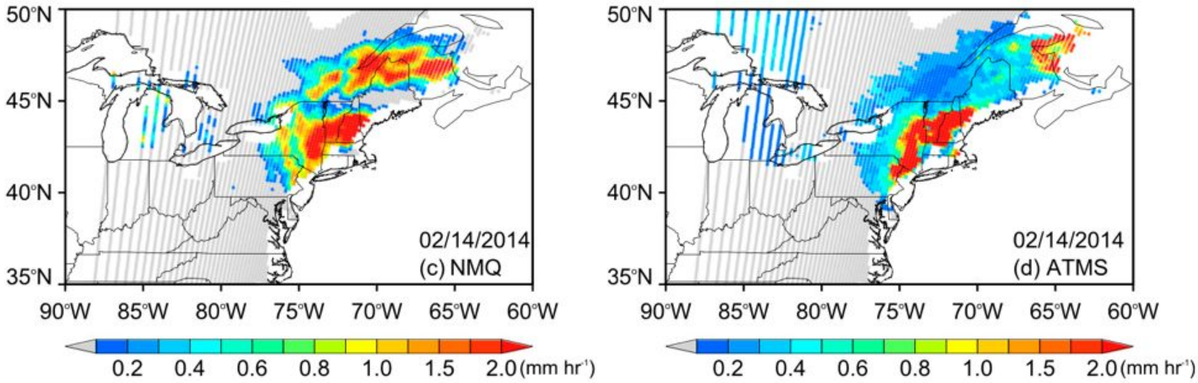

Figure 3.2.2 Snow event observed by NMQ (left) and by ATMS Bayesian algorithm by You et al. (2015) (right) on 14 Feb 2014 in the New England region (*from You et al., 2016*).

Noteworthily, these results are quite close to those inferred from the NOAA SFR algorithm shown in Figure 3.2.2 but the prototype method developed by You is able to well distinguish a U-shaped intense snowfall area over New England partially identified by the ground radars (NMQ).

In order to prevent these expected missed retrievals mainly due to the surface conditions during the storm, a hybrid algorithm has been conceived by Kongoli et al. (2018). In this work, the NOAA SFR computational scheme was supported by forecasts of a global model. Thus, the hybrid snowfall detection algorithm combines the statistical-based original scheme using AMSU-B/MHS/ATMS measurements with the output from a statistical analysis trained with in situ data that uses meteorological variables derived from NOAA's Global Forecast System (GFS) where the cloud thickness and relative humidity at 1 to 3 km height were the best predictors of snowfall occurrence.

A more physical hybrid approach developed to further improve the NOAA SFR algorithm performances (Kongoli et al., 2015, 2018) is experimented by Meng et al (2017, 2020). In this work the overland snowfall rate algorithm for PMW radiometers has been reinforced by a cloud properties analysis accomplished with a one-dimensional variational (1D-Var) model. The snowfall rate derived with the physical algorithm is further adjusted using a ground radar and gauge combined precipitation product. Both the snowfall detection and the snowfall rate algorithms have been validated respectively against ground observations and radar and gauge combined analyses from the contiguous United States.

In Figure 3.2.3 a comparison of only-satellite and hybrid approaches are presented. The portion of snowstorm observed by the U.S. National Radar Network is partially captured by satellite retrievals. Although both methods well identify the same snowy areas by discerning regions characterized by different snowfall regimes the satellite-only algorithm misses the circled areas over Illinois, Indiana and Ohio. On the contrary, the hybrid method performs better well identifying that region where the inferred snowfall rate is around 1.5 mm/hr corresponding to the radar reflectivity in the range 20 - 40 dBz.

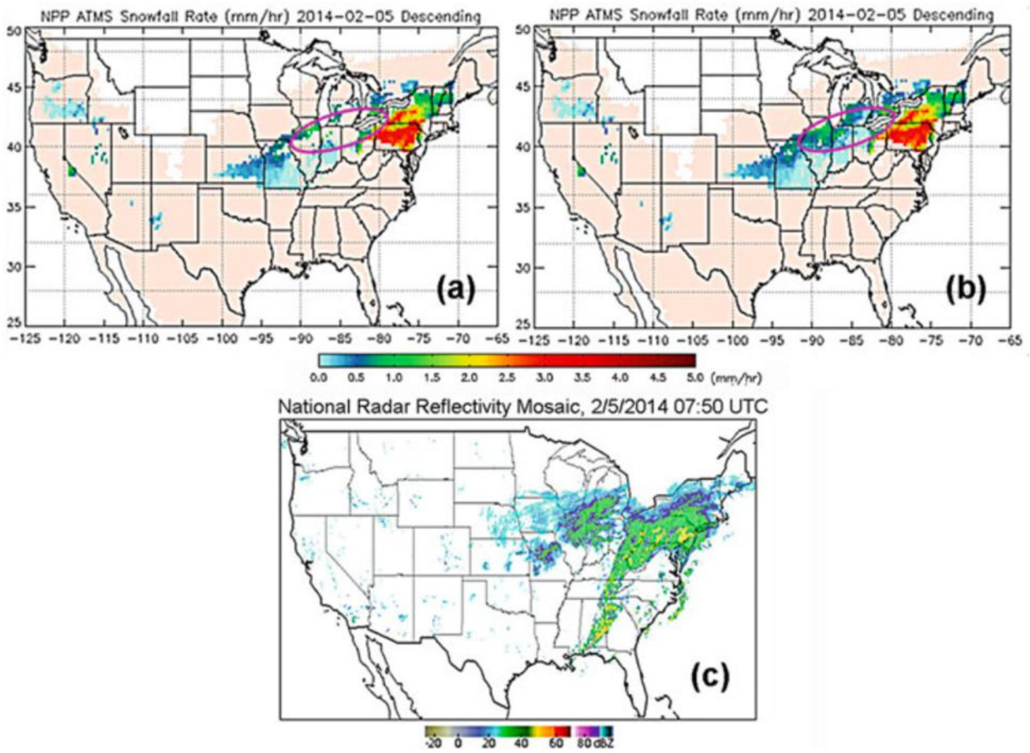

Figure 3.2.3: S-NPP ATMS SFR using (a) satellite-only algorithm, (b) hybrid algorithm, and (c) U.S. National Radar Composite reflectivity during the snowstorm on 5 February 2014 (*from Meng et al., 2020*).

3.2.2 Analysis of ATMS/CPR dataset: impact of background surface and supercooled water

Following the analysis of Takbiri et al. (2019) and Panegrossi et al. (2017), the analysis of the ATMS spectral signature in presence of snowfall has been carried out on the basis of the ATMS/Cloudsat coincidence database described in Section 3.1, mainly representative of higher latitudes snowfall systems (see Figure 2.2.2). In the database, two categories of snowfall elements have been created, one with supercooled water at the cloud top (as indicated by the DARDAR product, hereafter SLCT), and one snowfall without SLCT (although it may contain elements with supercooled droplets embedded in the cloud) (hereafter SN). Figure 3.2.4 shows the different distribution of snowfall elements in the two dataset categories, in terms of TPW and SWP (according to the CPR 2C-SNOW-PROFILE product). The SLCT snowfall elements are characterized by much lower SWP (< 0.5 kg m^{-2}) than the SN elements (up to 2.5 kg m^{-2}), whilehigher values of TPW are encountered for snowfall elements without supercooled water. Moreover, in order to analyze the ATMS spectral signature for different surface types, the ATMS frozen surface classification algorithm described in Section 5 has been applied to the dataset, thus identifying three predominant snow cover categories: *perennial snow*, *deep dry snow*, and *thin snow*.

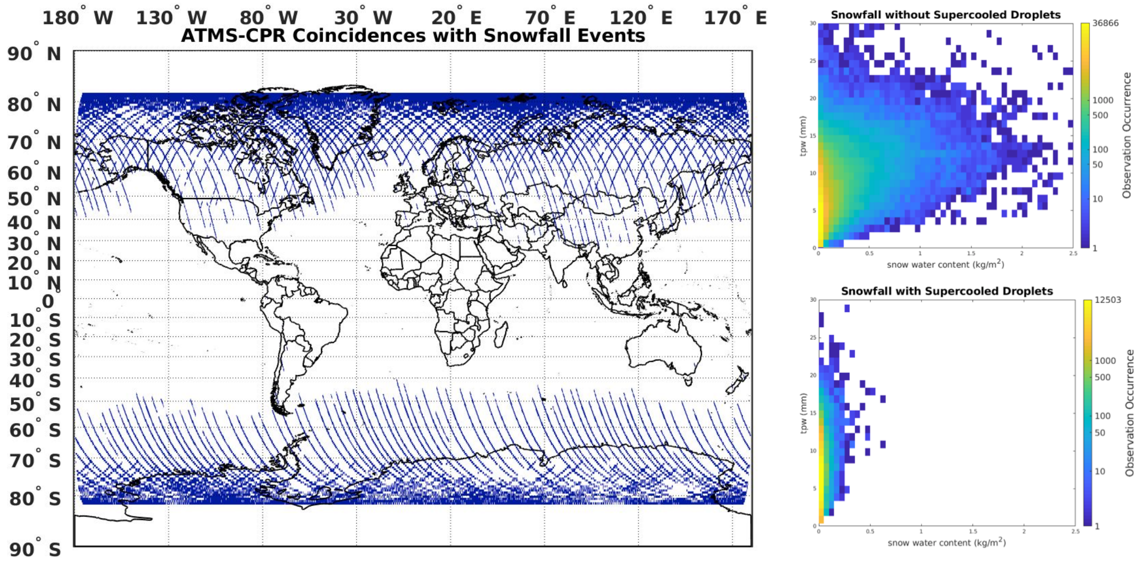

Figure 3.2.4: Analysis of ATMS/CloudSat coincidence dataset. Left panel: geographical distribution of snowfall elements. Right panel: scatterplot of TPW vs. CloudSat CPR columnar snow water content (or SWP, kg m^{-2}) for snowfall elements with and without supercooled water droplets at the cloud top.

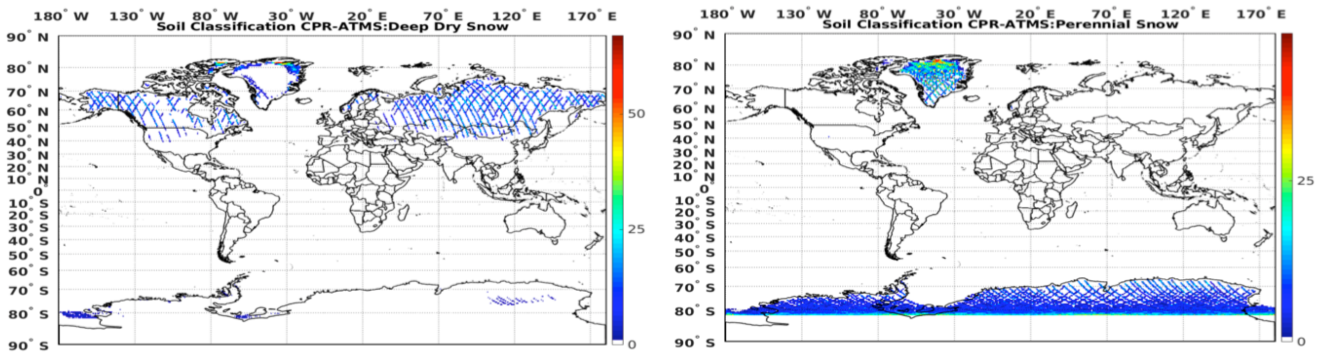

Figure 3.2.5: Geographical distribution of perennial snow (left) and deep dry snow (right) cover type in the ATMS/CloudSat coincidence dataset according to the ATMS surface classification algorithm described in Section 5.

The geographical distribution of deep dry snow and perennial snow in the ATMS/CloudSat dataset is shown in Figure 3.2.5. While perennial snow is mostly found over the Greenland Ice Sheet and Antarctica, deep dry snow is typically associated with higher latitude cold seasons and to the coasts of Greenland and Antarctica. Thin snow (not shown) is mostly seasonal snow found at mid latitudes.

Figure 3.2.6 shows the mean TBs for all ATMS channels (spectral signature) for the different background surface types, for the SLCT dataset elements (top panels) and without (SN, bottom panels). The spectral signature over land (vegetated, no snow) and over ocean (open water) are also shown for comparison. In each panel the curves represent the mean TBs for no snowfall CPR profiles, and for different classes of CPR 2CSP product snow water path (SWP = 0.05, 0.3, 0.6, 1.2 kg m^{-2}). For the SLCT category (top panels) only the two lowest SWP classes are found for perennial and deep dry snow, while for thin snow, land, and ocean higher SWP values are found. The TBs for the SN and SLCT elements show very different behaviour depending on the background surface, and as the SWP increases. Over *land*, and to a lesser extent over ocean, the scattering signal is evident for the SN elements, with increasing TB depression with respect to the no snowfall elements as SWP increases, mostly for the high frequency channels (> 165 GHz). A similar behavior is visible for *thin snow* for the 183.31GHz water vapour absorption band channels, less contaminated by the surface emission signal, while the other channels (including window channels at 88.2 and 165.5 GHz) show a complex behavior due to surface contamination. A very different behaviour is visible for the other radiatively colder snow cover categories. *For perennial snow* (radiatively colder than all other surface types) it is evident that TBs increase with respect to no-snowfall elements at all frequencies (also for very low SWP values 0.05 kg m^{-2}), but there is no variability of the TBs for SWP > 0.3 kg m^{-2}, likely because the atmospheric emission contribution (water vapour emission) balances the scattering effect of snowfall. Over *deep dry snow* (radiatively warmer than perennial snow and colder than thin snow), TBs increase as SWP increases mostly in the high frequency window channels (more at 165.5 GHz than at 88.2 GHz, in agreement with what was found for GMI by Takbiri et al., 2019), and, to a less extent, in the two least absorbing 183.31 GHz water vapour absorption band channels (183.31±7 and 183.31±4.5 GHz), more affected by the cloud contribution.

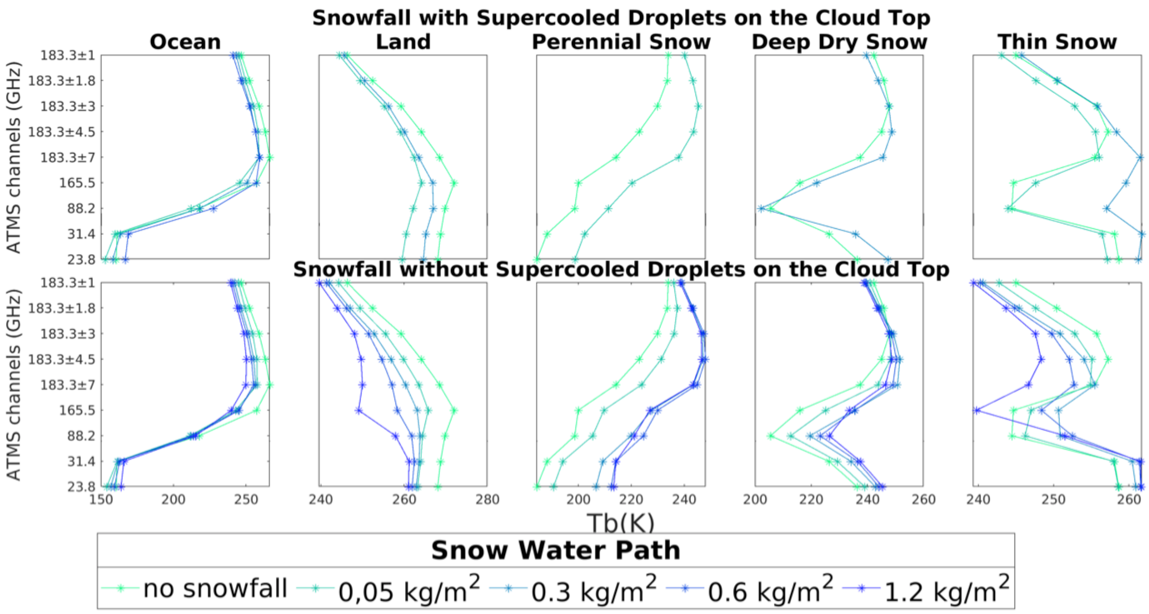

Figure 3.2.6: ATMS/CloudSat coincidence dataset mean brightness temperatures (TBs) for all ATMS channels (spectral signature) for different background surface types (ocean, vegetated land, perennial snow, deep dry snow, thin snow). The results are shown for all dataset elements with (top panels) and without (bottom panels) supercooled water droplets at the cloud top. In each panel the curves represent the mean TBs for no-snowfall CPR profiles, and for different classes of snow water path (SWP = 0.05, 0.3, 0.6, 1.2 kg m-2).

In presence of SLCT (top panels), similar ATMS spectral signatures of those obtained for SN (bottom panels) can be observed across the different surface types, but, depending on the SWP value (on average lower than for SN elements), the emission by cloud water droplets may reduce the TB depression (for example over land) or enhance the TB increase (for example over perennial snow). It is worth noting the different slope of the TB vector between 23.8 and 31.4 GHz for the different snow cover types, which is at the base of the ATMS frozen surface classification algorithm presented in Section 5.

As for GMI, another important element impacting the ability of ATMS high frequency channels to respond to the presence of snowfall is the water vapour content (TPW). Water vapour is the main contributor to atmospheric emission and, while on one side it masks the surface contribution to the upwelling radiation for a given channel, on the other limits the sensitivity of that channel to the cloud contribution (either the scattering effect by the frozen hydrometers and/or the emission effect by supercooled water droplets). Figure 3.2.7 shows the mean TBs at 165.5 GHz and at 183.3±7 GHz as a function of TPW for the three snow cover types analyzed in Figure 3.2.6 (thin snow, deep dry snow and perennial snow) and for no-snowfall dataset elements (CS), for different classes of snow water path (SWP = 0.05, 0.3, 0.6 kg m^{-2}) and for SLCT elements (with SWP = 0.05 kg m^{-2}). Overall, for a given SWP value the TBs increase almost monotonically with TPW (especially at 183.3±7 GHz), as expected. It is worth noting the scattering signal over thin snow for all SPW classes (TBs lower than no-snowfall TBs), except for the two lowest SWP classes where emission signal at 165.5 GHz is visible for TPW < 5 kg m^{-2} (mm).

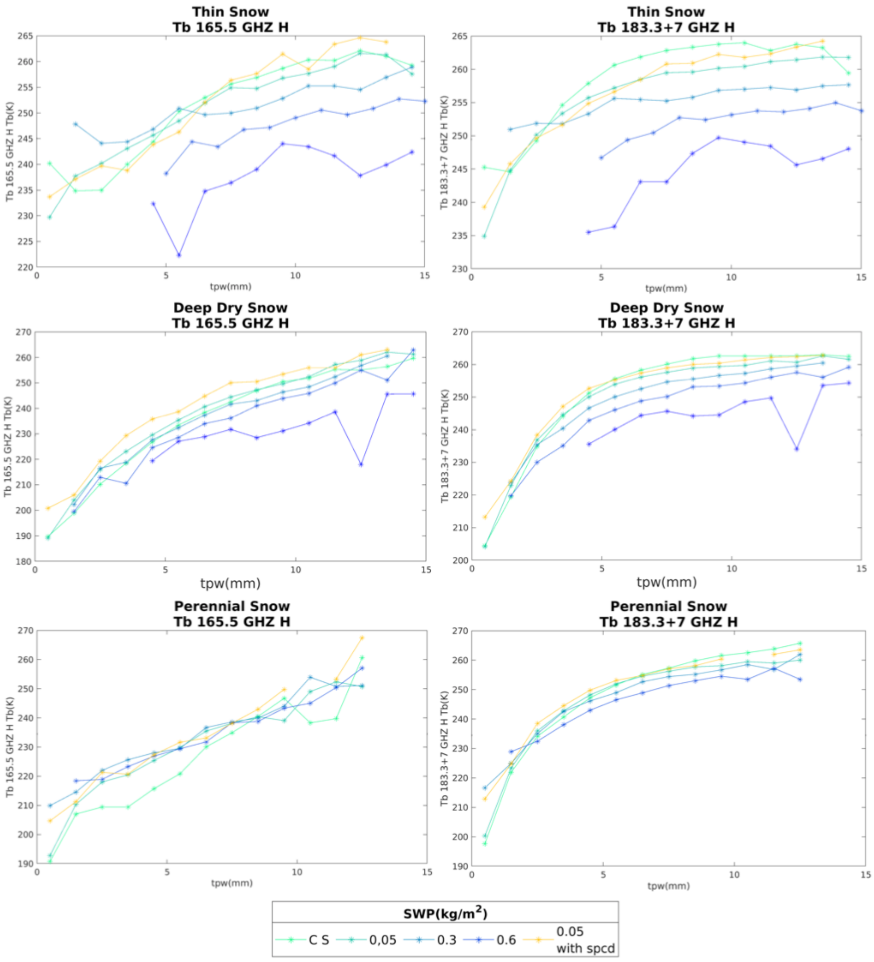

Figure 3.2.7: ATMS/CloudSat coincidence dataset mean brightness temperatures (TBs) at 165.5 GHz (left panels) and at 183.3±7 GHz (right panels) for different snow cover types (thin snow, deep dry snow and perennial snow) as a function of TPW. In each panel the curves represent the mean TBs for no-snowfall dataset elements (CS), for different classes of snow water path (SWP = 0.05, 0.3, 0.6 kg m-2), and for SLCT elements with SWP = 0.05 kg m-2 (yellow line).

Transitioning to deep dry snow, these signals become less evident. For perennial snow a significant emission signal (TB increase as high as 15 K) is observed for TPW < 8 kg m^{-2} (mm) for all SWP values, while for higher TPW the cloud contribution is no longer distinguishable from the no-snowfall curve. The prevalent emission signal for perennial snow and deep dry snow observed in Figure 3.2.6 is likely due to the fact low TPW is the predominant condition found in the polar regions (where perennial snow is found) and in the mid-latitude winter (usually characterized by deep dry snow). The effect of supercooled droplets at the cloud top is always to dampen the (very light) snowfall scattering effects on the TBs, reducing the TB depression, or increasing the TBs with respect to the no-snowfall (clear sky) condition.

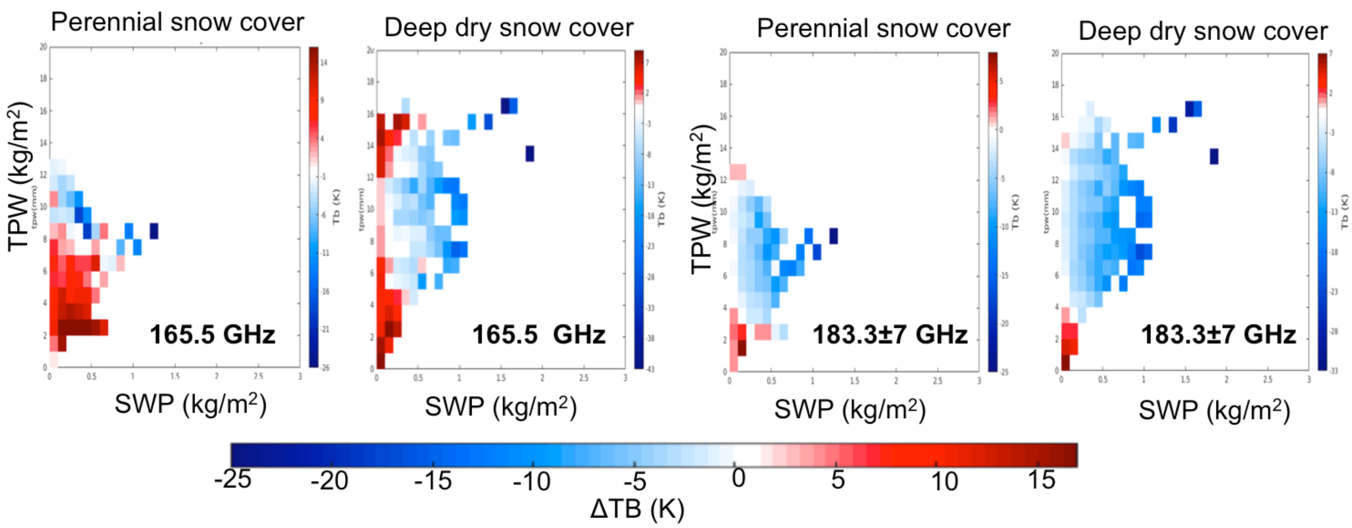

Figure 3.2.8: Mean difference of ATMS TB in presence of snowfall at 165.5 GHz and 183.3±7 GHz with respect to no-snowfall conditions (SWP=0 kg m^{-2}) in TWP/SWP bins for perennial and deep dry snow in the CloudSat/ATMS dataset.

The different behaviour of the 165.5 GHz and 183.3±7 GHz over perennial snow and deep dry snow is clearly evidenced in Figure 3.2.8, showing the mean difference between snowfall ATMS TBs and no-snowfall (SWP = 0.0 kg m^{-2}) TBs for the CloudSat/ATMS dataset elements sorted in different 2-D bins of TPW and SWP. The emission signal (positive TB difference) is represented in red, and a scattering signal (negative TB difference) in blue. While a scattering signal is always observed at 183.3±7 GHz except for very low values of TPW for both surfaces, a transition from emission signal to scattering signal is evident at 165.5 GHz over perennial snow (for TPW ~ 8 kg m-2) and dry snow (for TPW ~ 5). Over dry snow it is also interesting to note the transition from positive to negative TB difference for larger values of TPW as SWP increases, i.e., when the scattering from the frozen hydrometeors dominates over the atmospheric emission.
In summary, over thin snow cover, the dominant snowfall signal is due to its scattering at the high-frequency channels, although less evident than over vegetated land, that can become an emission signal in presence of supercooled water. When surface emission is significantly reduced (over the dry snow and perennial snow), an emission signal is observed, chiefly in response to the increased water vapour paths (see Liu and Seo 2013; You et al. 2016), or to the presence of supercooled water. This emission signal, which leads to higher TBs, indirectly indicates the likelihood of precipitation. The correct interpretation of the departure from the clear-sky values of the ATMS-based multi-frequency TB observations in presence of snowfall is mandatory to improve snowfall retrievals not only over dry snow (as shown for GMI in Section 3.1) but also over perennial snow at very high latitudes and polar regions. However, this requires as a prerequisite the correct identification of the background surface conditions and the detection of supercooled droplets.